AGU PUBLICATIONS

JGR

Journal of Geophysical Research: Oceans

RESEARCH ARTICLE

10.1002/2014JC009943

Key Points:
- Examines snow depth of Weddell and Bellingshausen Seas
- Snow depths generally higher than those from in situ records
- Implications on sampling and our view of Antarctic snow depth

Correspondence to:
R. Kwok,
ronald.kwok@jpl.nasa.gov

Citation:
Kwok, R., and T. Maksym (2014), Snow depth of the Weddell and Bellingshausen sea ice covers from IceBridge surveys in 2010 and 2011: An examination, *J. Geophys. Res. Oceans*, *119*, 4141–4167, doi:10.1002/2014JC009943.

Received 5 MAR 2014
Accepted 13 JUN 2014
Accepted article online 16 JUN 2014
Published online 8 JUL 2014

Snow depth of the Weddell and Bellingshausen sea ice covers from IceBridge surveys in 2010 and 2011: An examination

R. Kwok[1] and T. Maksym[2]

[1]Jet Propulsion Laboratory, California Institute of Technology, Pasadena, California, USA, [2]Woods Hole Oceanographic Institution, Woods Hole, Massachusetts, USA

Abstract We examine the snow radar data from the Weddell and Bellingshausen Seas acquired by eight IceBridge (OIB) flightlines in October of 2010 and 2011. In snow depth retrieval, the sidelobes from the stronger scattering snow-ice (s-i) interfaces could be misidentified as returns from the weaker air-snow (a-s) interfaces. In this paper, we first introduce a retrieval procedure that accounts for the structure of the radar system impulse response followed by a survey of the snow depths in the Weddell and Bellingshausen Seas. Limitations and potential biases in our approach are discussed. Differences between snow depth estimates from a repeat survey of one Weddell Sea track separated by 12 days, without accounting for variability due to ice motion, is -0.7 ± 13.6 cm. Average snow depth is thicker in coastal northwestern Weddell and thins toward Cape Norvegia, a decrease of >30 cm. In the Bellingshausen, the thickest snow is found nearshore in both Octobers and is thickest next to the Abbot Ice Shelf. Snow depth is linearly related to freeboard when freeboards are low but diverge as the freeboard increases especially in the thicker/rougher ice of the western Weddell. We find correlations of 0.71–0.84 between snow depth and surface roughness suggesting preferential accumulation over deformed ice. Retrievals also seem to be related to radar backscatter through surface roughness. Snow depths reported here, generally higher than those from in situ records, suggest dissimilarities in sample populations. Implications of these differences on Antarctic sea ice thickness are discussed.

1. Introduction

In the 34 year satellite record (1979–2012), the total extent of Antarctic sea ice has increased at an average rate of ~1.5% per decade [*Vaughan et al*., 2013], but with strong regional differences that range from −4.3% per decade in the Bellingshausen/Amundsen Sea sector to 4.3% per decade in the adjacent Ross Sea sector. Ice extent, however, provides only a limited picture of sea ice response to climate change and variability; changes in regional distributions of ice thickness and volume may be better measures. At this time, measurements of Antarctic sea ice thickness are too few to be able to judge whether the total volume (mass) of the ice cover is decreasing, steady, or increasing.

Models suggest significant changes in ice volume and thickness have accompanied ice extent changes [*Massonnet et al*., 2013], and recent increases in ice thickness may have been greater than the corresponding increases in extent [*Zhang*, 2014]. However, coupled models generally do not capture observed trends and variability in the Antarctic [*Maksym et al*., 2012; *Turner et al*., 2013]. Satellite altimeters cannot yet determine ice thickness reliably in the Antarctic, largely due to uncertainties in snow depth [e.g., *Giles et al*., 2008]: snow loading is required for conversion of freeboard to thickness. In recent efforts to determine sea ice thickness using various estimates of the snow depth, a wide discrepancy between ice thickness estimates persists [*Yi et al*., 2011; *Kurtz and Markus*, 2012; *Xie et al*., 2013]. Such estimates are necessary to evaluate both stand-alone sea ice and coupled climate models, attribute the causes of recent observed changes, and to evaluate and improve understanding of physical processes controlling sea ice extent and thickness and hence improve model projections of the future sea ice cover. For instance, many of the processes thought to contribute to Antarctic sea ice extent trends may be more directly observable through their impact on ice thickness (e.g., thickening due to increased precipitation and snow ice formation, increased ocean stratification, or increased deformation).

Current algorithms to derive ice thickness from ICESat (Ice, Cloud, and land Elevation Satellite) rely on either an independent measure of snow depth [*Yi et al*., 2011], assume that the snow depth is equal to the ice

freeboard [*Kurtz and Markus*, 2012], or use empirical relationships between total freeboard and ice thickness [*Xie et al*., 2013]. The first of these is limited due to underestimates of snow depth in areas of deformed ice [*Markus et al*., 2011]. The second assumption may be more appropriate for the thinner, outer pack where ice freeboards may be only a few centimeters. For thicker ice, the third method may be most suitable, as the need to know densities and ice freeboard is reduced. However, such empirical relationships vary seasonally and regionally [*Ozsoy-Cicek et al*., 2013], and so the associated uncertainty limits the ability to detect thickness changes. Nevertheless, these investigations have provided the best large-scale estimates of the spatial variability of the ice and snow cover based on our present knowledge. In all, because of the importance of snow depth in sea-ice mass balance, in the surface heat and energy budget, and in ice thickness retrieval, remote determination of snow depth at almost any spatial scale has long been desired.

NASA's Operation IceBridge (OIB) [*Koenig et al*., 2010] was implemented as an airborne remote sensing program to extend the laser altimeter time series through the gap between the end of ICESat data collection in 2009 and the launch of the ICESat-2 lidar in 2016. The airborne instrument suite includes an ultrawideband radar for measuring snow depth. This OIB snow radar is an improved version of earlier ground-based systems designed and built at CReSIS [*Wilyard*, 2006; *Panzer et al*., 2013]. The ground-based radar (2–8 GHz bandwidth) was tested on Antarctic sea ice during the austral summer of 2003 [*Kanagaratnam et al*., 2007]. Since 2009, OIB has flown surveys for acquiring spring data over the Arctic and Antarctic sea ice cover. Early assessment of some of these data sets of the Arctic can be found in *Farrell et al*. [2011], *Kurtz and Farrell* [2011], and *Kwok et al*. [2011]. Analysis of the Antarctic data acquired by this snow radar is the subject of this paper. In particular, we examine the effect of sidelobes from the stronger scattering snow-ice (s-i) interface on the detection of the weaker air-snow (a-s) interface; this effect was noted in *Kwok et al*. [2011] but has not been accounted for in current retrieval approaches. Here, we introduce a retrieval approach that mitigates the impact of the radar system impulse response (SIR) that is controlled by parameters adapted to different radar SIRs, followed by a survey of the snow depths in the Weddell and Bellingshausen Seas.

The paper is organized as follows. Section 2 describes the instruments and the data sets used in the following analyses. Section 3 shows examples of radar returns from the snow cover, discusses the effects of system sidelobes in the detection of air-snow interfaces, and describes a retrieval approach for mitigating such effects. Section 4 gives an assessment of the retrievals with repeat tracks acquired in the Weddell Sea. With the methodologies developed in section 4, we examine the regional distribution of the retrieved snow depth in the flights over the Weddell and Bellingshausen Seas in section 5. Section 6 examines the retrievals within the context of available observations and revisits the useful geophysical results from our analysis. Summary remarks and conclusions are provided in the last section. Section 3 deals primarily with remote sensing issues and may be skipped for readers interested in only the snow depth results.

2. Data Description

Data sets from Operation IceBridge (OIB) are archived at the National Snow and Ice Data Center (NSIDC). Of the suite of OIB instruments, the two instruments of interest in this paper are the ultrawideband radar used to produce snow depth estimates and the Airborne Topographic Mapper (ATM—a lidar) employed to provide high-precision elevations of the snow cover. These instruments are operated simultaneously and provide near-coincident coverage, albeit at different spatial resolutions. In this section, we provide a brief description of the performance and coverage of the radar and lidar systems.

2.1. Snow Radar

This frequency-modulated continuous-wave (FM-CW) radar is operated by the Center for Remote Sensing of Ice Sheets (CReSIS) at the University of Kansas. First flown on the Arctic OIB campaign in the spring of 2009, improved implementations have been employed for subsequent Arctic and Antarctic campaigns. Radar parameters used during the 2010 and 2011 campaigns (in Table 1) show that the radar characteristics are substantially the same. A bandwidth of 2–6.5 GHz combined with a sweep duration of 250 μs provides a range resolution of $\sim$5 cm (in free space) for resolving the location of the air-snow (a-s) and snow-ice (s-i) interfaces. The pulse repetition frequency controls the interval between subsequent transmitted pulses and thus the spatial separation between radar spots on the ground. With averaging, the spot separation is $\sim$1 m along track at an altitude of $\sim$500 m and an air speed of $\sim$250 kts (the nominal flight parameters for all OIB

Table 1. Snow Radar Parameters

Radar Parameter	2010	2011
Bandwidth (GHz)	2–6.5	2–6.5
Pulse Length (μs)	250 or 255	250 or 255
Pulse Repetition Frequency (kHz)	2	2
Transmit Power (dBm)	20	20
IF Frequency Range (MHz)	31–62	31–62
Sampling Frequency (MHz)	62.5	62.5
Range Resolution (free space) (cm)	~5	~5

sea ice surveys). When coherent reflections from relatively smooth surfaces as those from the a-s and s-i interfaces dominate, the size of the footprint can be approximated by the radius of first Fresnel zone (i.e., $8.657\sqrt{2d/f}$ in meters). In the equation, d is the distance (in kilometers) to the surface and f is the highest frequency (in GHz) of the radar's bandwidth. With $d = 0.5$ km and $f = 6.5$ GHz, the footprint diameter is ~6.7 m. The reader is referred to the published literature for a more detailed description of the radar system [*Kanagaratnam et al*., 2007; *Wilyard*, 2006; *Patel*, 2009; *Panzer et al*., 2013].

The 2010 snow radar data are distributed in individual files each containing ~4000 radar echograms with a nominal ground separation of ~1 m between echograms. The 2011 data, with an additional incoherent averaging of five radar returns along track to reduce noise, contain only 1000 echograms with a separation ~4 m between averaged echograms. We do not find any notable differences between these products in our present analysis. Henceforth, we refer to these individual files as radar segments.

2.2. ATM Lidar

The ATM is a conical-scanning laser ranging system operated at a wavelength of 532 nm with a pulse repetition frequency of 5 kHz and scan rate of 10 Hz with an off-nadir scan angle of 15° [*Krabill et al*., 2002]. With the nominal OIB flight parameters described above (i.e., operating altitude and ground speed: 500 m and 250 kts), the ATM observation geometry provides an across-track scan swath of ~250 m with the laser illuminating a 1 m diameter footprint sampled approximately every 3–4 m along-track and across-track near the center of the scan swath. The sampling is denser (submeter) near the edges of the swath due to the conical scanning geometry of the system.

The recorded waveform from the snow or ice surface is used to measure the time delay of a return signal and determine a total propagation distance. The presence of extremely smooth surfaces along the flight path typically results in some measurement dropouts, probably due to the forward scattering of the lidar pulse. The travel time data are combined with GPS navigation measurements and aircraft orientation parameters to derive surface elevation measurements relative to the WGS84 reference ellipsoid; accuracy is typically better than 10 cm [*Krabill et al*., 2002]. The ATM elevations are provided in data files that cover tracks of ~35 km.

2.3. Other Data Sets

Synthetic aperture radar (SAR) mosaics of the Weddell Sea are constructed with ESA's Envisat SAR imagery (HH-mode). The Envisat ice motion fields used here were derived using a procedure described by *Kwok et al*. [1990]. Surface air temperature fields are from European Centre for Medium-Range Weather Forecasts (ECMWF).

3. Retrieval of Snow Thickness

This section is divided into four parts. First, we provide an example illustrative of radar returns from the snow cover. Second, we discuss the detection of the air-snow (a-s) and snow-ice (s-i) interfaces and the effects of embedded sidelobes in the radar profiles. Third, an approach to address the impact of sidelobes, that may be relevant to both Antarctic and Arctic data sets, is suggested. Sidelobes are not explicitly addressed in the current operational IceBridge retrieval procedures [*Kurtz et al*., 2013]. Lastly, we discuss the limitations of our approach.

3.1. Character of Radar Returns

A radar/lidar composite in Figure 1 shows the mix of radar returns from a 4 km segment over the southern Weddell ice cover. The radar and lidar data are synchronized to a common GPS signal on the aircraft. The a-s and s-i interfaces can be seen as distinct peaks in the echo profiles (examples in Figure 1d). In each

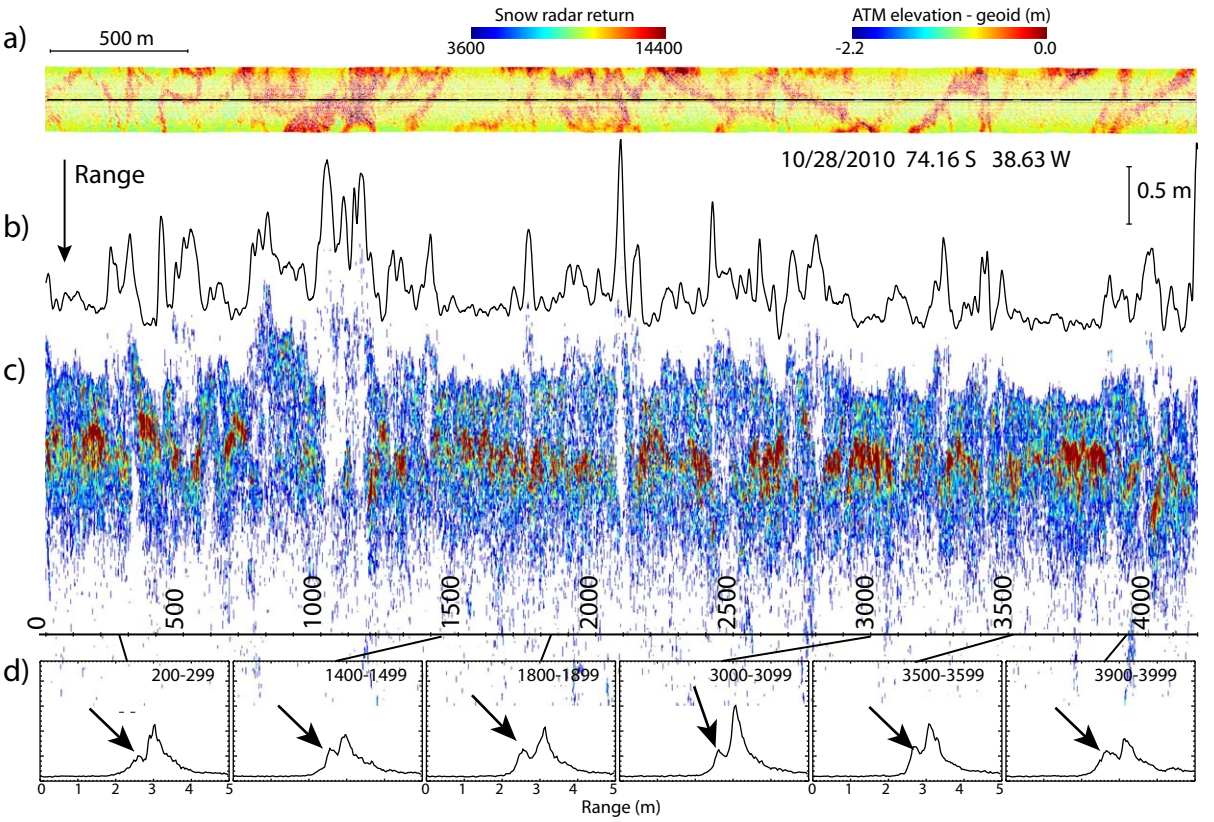

Figure 1. A 4 km segment of ATM lidar and snow radar data from the IceBridge flight on 28 October 2010. (a) ATM lidar swath (~250 m; color-coded elevation) with the snow radar track (black-dashed line) near the center of the lidar swath. (b) Profile of lidar elevation associated with each snow radar footprint of ~7 m. (c) Range-varying backscatter along the snow radar track (high backscatter in red). Range direction is shown on the left side of the figure. (d) Radar profiles (average of 100 snow radar returns) from six locations along the track. Radar backscatter magnitudes are uncalibrated, so only the relative magnitudes are meaningful. Center location of radar segment is 74.16°S and 38.63°W. Ocean tides and EGM2008 geoid have been removed from the ATM elevations.

profile, there is a distinct leading edge in response to the transition from the air to snow volume; followed by a peak that is the location of the a-s interface (indicated by arrows in Figure 1d). The highest unambiguous peak in the profile is typically the return from the s-i interface. Between the peaks, returns may be due to sidelobes or scattering from internal layers within the snow volume as demonstrated with ground-based systems [*Kanagaratnam et al.*, 2007]. Past the trailing edge of the s-i peak, returns are from off-nadir surfaces or volume (or clutter) beyond the range to the s-i interface; the angular (or time) extent of these returns is determined by the backscatter from the surface and the antenna beamwidth.

The echograms in Figure 1c also show that magnitudes of s-i peaks (in red) are distinctively higher than that from the snow surface (thin green-red peaks seen above the strong s-i peak). Under certain conditions, however, the strengths of the returns are low and appear as data gaps [*Kwok et al.*, 2011]. This is often seen in areas with significant surface relief: examination of the ATM elevation field (Figure 1a) shows that this phenomenon is associated with pressure ridges or deformed ice (indicated in red). When the pulse-to-pulse returns vary significantly or decorrelate over short distances, coherent averaging of the returns (part of the data collection process) reduces signal strength. For example, one expects this over sea ice ridges with base-widths of only several meters (compared to ground sampling intervals of the radar) or asymmetric snowdrifts with significant surface slopes. In these cases, a well-defined layer of snow over a flat ice surface may not exist and coherence is thus reduced. The absence of snow at the crests of pressure ridges is also a confounding effect.

Returns with the highest signal strength (or signal-to-noise ratio) allow a more quantitative examination and visualization of the radar's range resolution and the expected level of the system sidelobes.

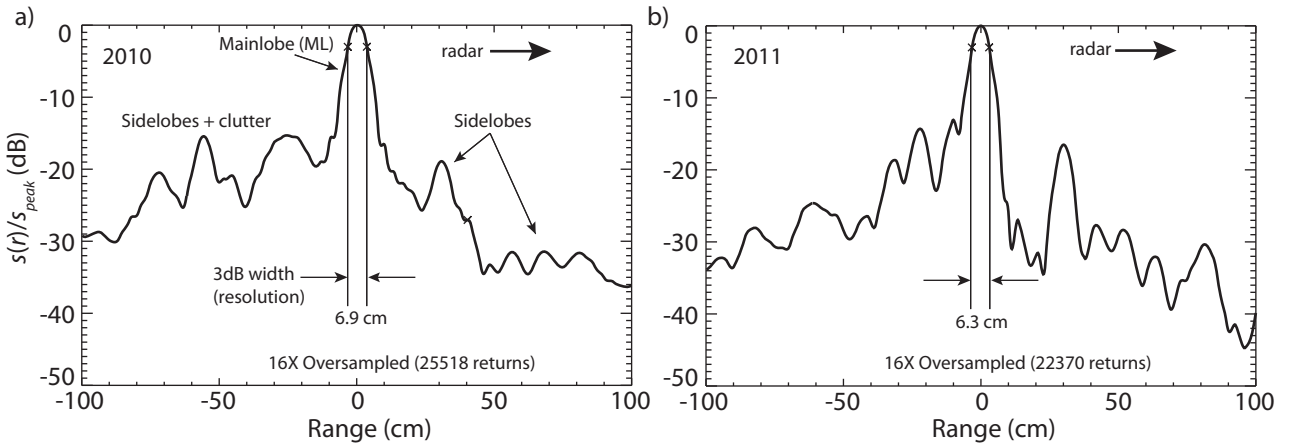

Figure 2. Average sidelobe structure of the radar returns from quasi-specular surfaces, i.e., very smooth surfaces. (a) October 2010. (b) October 2011. Range resolution of the radar is the width of the mainlobe (ML) at 3 dB below the level of the peak. Each profile is the average of the top 10% of the radar returns from that day (oversampling factor: 16).

The average of the highest 10% of the radar returns (see Figure 2) show a profile that is asymmetric in range with trailing edge clutter (discussed above); the structure and the levels of the sidelobes are different for the 2 years. The range resolution of the system, typically defined as the width of the mainlobe at a level 3 dB below the peak, is ∼6.9 and ∼6.3 cm in 2010 and 2011, respectively. As a result of sidelobe suppression in the output and variability in the actual returns, the observed resolutions are always broadened from the theoretical limit of ∼5 cm (in Table 1). While the width of the mainlobe is a measure of range resolution, it is useful only when the return signal strength from the two interfaces are comparable. When the scattering from the s-i interface is much stronger than that from the a-s interface, the detectability of the weaker return could be masked by the stronger mainlobe of the s-i return (especially if the separation between the interfaces is small), or by its sidelobes in cases when the return of the a-s interface is weak.

3.2. Interface Detection and Radar Sidelobes

To obtain snow depth from a given sampled radar profile, $s(i)$ requires the identification of the range locations of the a-s and s-i interfaces. In our retrieval process, the highest return in a radar profile ($s_{peak} = \max_{i\in 1\ldots N_s} s(i)$) is designated as the return from the s-i interface; this is the fundamental assumption of our approach. While field studies with Ku-band radar have shown that internal layering and wetness in the snow can cause radar returns from within the snowpack, obscuring the s-i interface [*Willat et al*., 2011], the only field study with wideband radar in the Antarctic [*Kanagaratnam et al*., 2007] showed consistent strong returns from the s-i interface, even when internal layering was present. A correlation of 0.95 between radar and measured snow depth with no bias was found for cold snow ($<-5^{\circ}$C). Wetness in warmer snow, or more substantial layering (e.g., icy melt layers) are expected to make unambiguous detection more difficult. In most cases, however, the primary challenge is in the unambiguous identification of the weaker returns from a-s interfaces that is embedded in noise, system artifacts, and other effects.

To find the significant peaks in $s(i)$, we first define:

$$\Delta(i) = |s(i+1) - s(i)|,$$

as a measure of sample-to-sample variability. The mean of Δ (i.e., $\bar{\Delta}$) and positive root-mean-squared deviations from $\bar{\Delta}$ (i.e., δ^{+}_{RMS}) are computed using the noise data in the first 100 samples of all the radar profiles within each 4 km snow radar data file. δ^{+}_{RMS}, the tail of the positive-valued asymmetric distribution of Δ, is used as a measure of deviation from the mean. We deem a sample at range location i to be a statistically significant local maximum/peak when the following conditions (C_1 and C_2) are met:

$$C_1 : (s(i) > s(i-1)+t) \wedge (s(i) > s(i+1)+t)$$
$$C_2 : (s(i) > s(i-2)) \wedge (s(i) > s(i+2))$$

and where $t=\bar{\Delta}+2\delta^{+}_{RMS}$. The first condition ($C_1$) defines the required excursion of the signal level above the adjacent samples and the second condition (C_2) requires the signal level to be higher than the signal levels one sample removed from $s(i)$, i.e., $s(i\pm2)$.

With this simple peak retrieval scheme, we select the first significant near-range peak encountered by the radar (i.e., farthest from the s-i interface) as the location of the a-s interface. Taking the range separation between the a-s and s-i interfaces to be Δr ($=r_{a-s}-r_{s-i}$), we obtain distributions of retrieved Δr in Figure 3b (filled histograms). The anomalous spikes in the distributions of Δr from two selected flight lines (one each from 2010 and 2011) are quite striking (see Figure 3b). Examination of the distribution of population of detected peaks as a function of location and signal level (Figure 3c) shows that noticeable populations are concentrated at those locations and signal levels where sidelobes are found (in Figure 3a—relative to mainlobe peak, s_{peak}). For instance, the higher density of population of peaks at (18 dB, 30 cm) in Figure 3c (left) is due to the first sidelobe of the s-i response in Figure 3a (left), in which the normalized radar returns ($\tilde{S}(i)=s(i)/s_{peak}$) are plotted. Each curve (i.e., $\tilde{S}(i)=s(i)/s_{peak}$) is constructed from echograms averaged over a 1 dB interval of peak-signal-to-noise levels ($PSNR=s_{peak}/\bar{n}$). Clearly, the spikes in the one-dimensional distributions (in Figure 3b) are associated with the sidelobes that have been mistaken for real surface returns in the detection process.

These detection errors would bias the distribution means and variances. The larger number of spikes in the Δr distribution on 18 October 2011 is due to higher and more distinct sidelobes in the radar system response: the strongest sidelobe on 18 October 2011 is 4 dB higher than the strongest one on 30 October 2010. Accounting for and understanding the effect of the system sidelobes are therefore important in any approach for reliable detection of the a-s interface.

Sidelobes are characteristics of the system response and have three features of note (see Figure 3a): (1) they are distinct and better defined when the returns from the s-i interface are strong; (2) their levels (relative to the mainlobe) generally decay with distance from the s-i return; and (3) in the case of the IceBridge snow radar, they remain stationary during a given campaign unless changes are made to the radar hardware. Figure 3a illustrates these three sidelobe features in the radar returns from 30 October 2010 to 18 October 2011. It can be seen that sidelobe visibility, and therefore, the potential impact on peak detection, is dependent on the peak return or the signal-to-noise level of the s-i return in the radar profile ($PSNR=s_{peak}/\bar{n}$). As the $PSNR$ decreases, the sidelobes become buried in the noise and become less of an impact on peak detection; however, this is not a desirable scenario as it reduces the system sensitivity to weaker returns from the a-s interface. Further, sidelobe levels are typically higher with proximity to the s-i peak although their locations do not vary with signal strength.

Also important to note are the differences in the range-varying nature of the sidelobes and their levels between the 2 days. As mentioned earlier, the highest sidelobe on 18 October 2011 is 4 dB higher than the highest one on 30 October 2010. Also, the number, locations, as well as their sharpness differ. Even though the general radar parameters remain unchanged (Table 1), any modification to the snow radar hardware (e.g., antennas, electronics, etc.) with every installation on the aircraft platform alters the structure of the sidelobes. These are difficult to control although every effort is made to minimize the level of especially the first sidelobe.

3.3. Detection of the Air-Snow Interface: An Approach

Here, we introduce several criteria that seem effective in reducing the signal-dependent and range-varying effects of system sidelobes. The results from applying this procedure can be seen in Figure 3d; the anomalous spikes in the retrievals (in Figure 3b) are suppressed and no longer visible.

The approach is as follows. For a given candidate peak, $\tilde{s}_{can}(i)\quad(=s_{can}(i)/s_{peak})$ detected using the above procedure to be designated as the a-s return, we add the following conditions (C_3 and C_4):

$$C_3:\tilde{s}_{can}(i)>\tilde{S}(i;PSNR)+t'(\tilde{S}(i;PSNR),PSNR)\quad\text{in dB}$$

$$t'=\begin{cases}a(PSNR) & \tilde{S}(i;PSNR)>-15\,\text{dB}\\ a(PSNR)\cdot(20+\tilde{S}(i;PSNR))/5 & -20\,\text{dB}\le\tilde{S}(i;PSNR)\le-15\,\text{dB}\\ 0 & \tilde{S}(i;PSNR)<-20\,\text{dB}\end{cases}$$

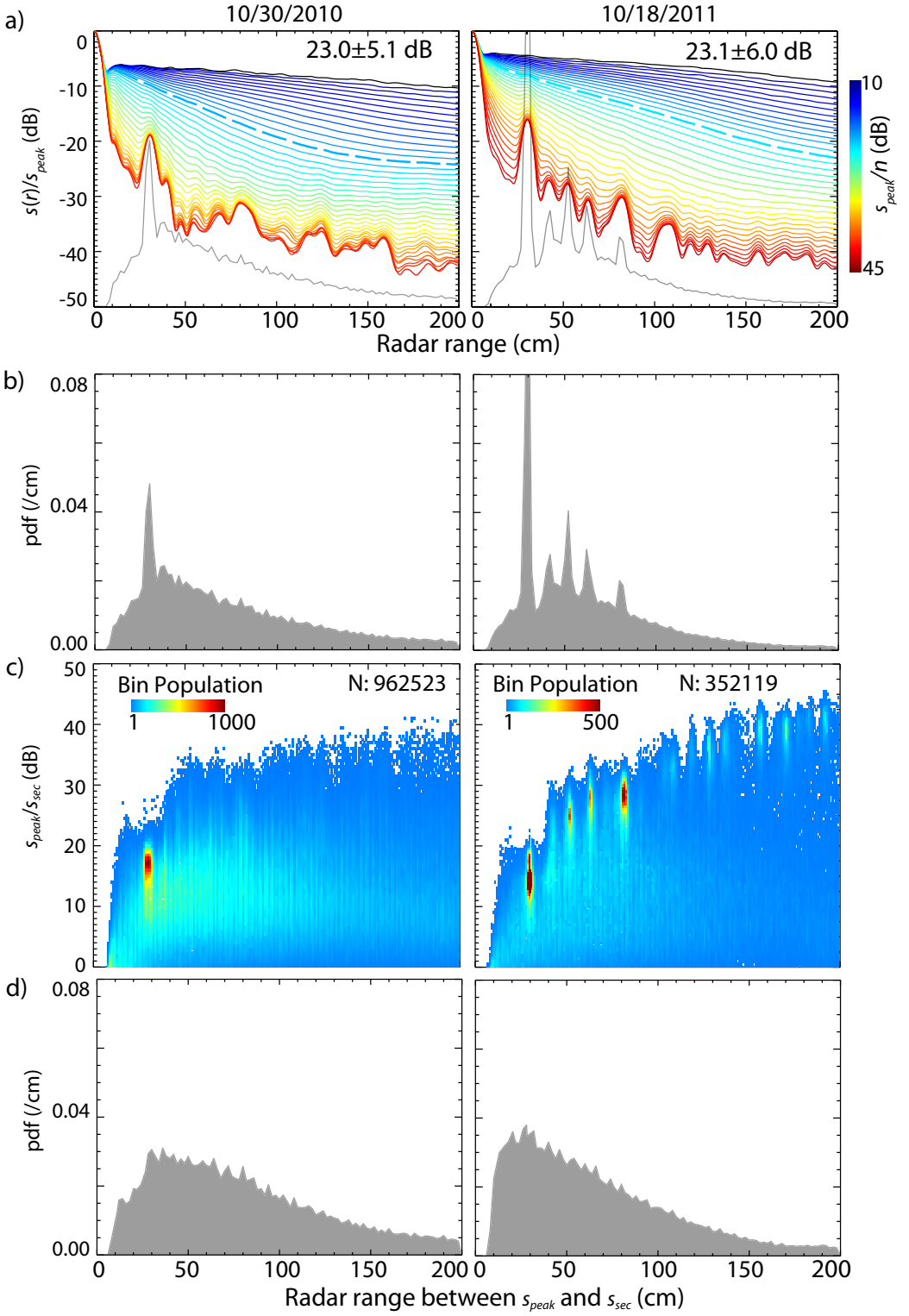

Figure 3. Impact of sidelobe level and structure on a-s peak detection. (a) Average of normalized returns ($\bar{s}=s(i)/s_{peak}$) at different peak-signal-to-noise levels ($PSNR=s_{peak}/\bar{n}$) from all radar profiles on 30 October 2010 and 18 October 2011. Normalized returns ($\bar{s}$) are for every 1 dB increment of *PSNR* between 10 and 45 dB. The mean and standard deviation of *PSNR* of the each population are shown in the top right corners of each plot. (b) Distribution of detected secondary peaks without considering the effects of sidelobes, this is also shown as gray line in plot a. (c) Population of detected secondary peaks and their levels (relative to s_{peak}) as a function of their range distance from s_{peak}. (d) Distribution of detected secondary peaks after accounting for the effects of sidelobes. Detected secondary peaks are candidate locations of the air-snow surface.

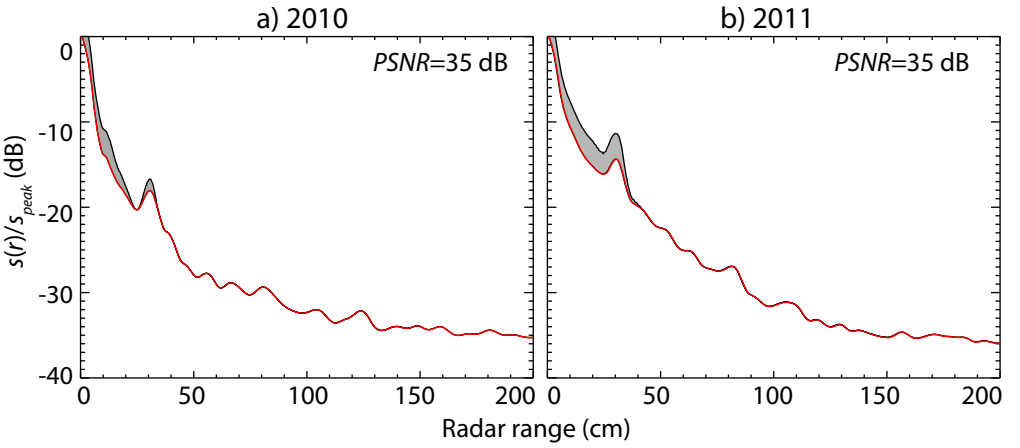

Figure 4. Threshold levels for selection of candidate peaks for $PSNR = 35$ dB. (a) 2010. (b) 2011. $\tilde{S}(i;PSNR)$ is in red, and the green/red line represents $\tilde{S}(i;PSNR)+t'(\tilde{S}(i;PSNR),PSNR)$ (see text for description).

$$a(PSNR)=\begin{cases} T & PSNR > 20\,\text{dB} \\ T\cdot(PSNR-10)/10 & 10\,\text{dB} < PSNR \le 20\,\text{dB} \end{cases}$$

$$C_4: -1\text{dB} > \tilde{s}_{can}(i) > -15\,\text{dB}$$

$$C_5: \text{ Select } \tilde{s}_{can}(i-1) \text{ if } \tilde{s}_{can}(i-1) > \tilde{s}_{can}(i) \text{ and separation between peaks is expected distance between main and sidelobes}$$

C_3 requires the level of $\tilde{s}_{can}(i)$ to be higher than $\tilde{S}(i;PSNR)+t'$, where $\tilde{S}(i;PSNR)$ is the average of normalized radar returns ($\tilde{S}(i)=s(i)/s_{peak}$) for a given $PSNR$ (where $PSNR=s_{peak}/\bar{n}$). That is, $\tilde{S}(i;PSNR)$ is a family of curves (see Figure 3a) and, in our case, each curve represents averages of echograms over 1 dB increments of $PSNR$ between 10 and 45 dB, i.e., there are 36 such curves. t' is determined by the $PSNR$ and the level of $\tilde{S}(i;PSNR)$ at range location i. The dependence of t' on these two variables addresses the need to consider strength of the sidelobes associated with the level of the s-i return, and their range-varying sidelobe structure for different radar installations. Figure 4 shows examples of $\tilde{S}(i;PSNR)+t'$ when $PSNR = 35$ dB.

In our procedure, t' is set to zero when $\tilde{S}(i;PSNR) < -20$ dB, i.e., when the expected effects of sidelobe levels are negligible. t' is dependent on $a(PSNR)$ when the $PSNR > 10$ dB. $a(PSNR)$ provides the overall signal strength-dependent suppression of the range-varying sidelobes; it increases from zero to its maximum value T, between $PSNR = 10$ and 20 dB. Increases in t' increase the suppression of the more distinct sidelobes in the returns when the $PSNR$s are higher. As seen in Figure 3a, the visibility and strength of sidelobes are high when the $PSNR$s are high and vice versa. The magnitude of t' is also dependent on the location of the candidate peak $\tilde{s}_{can}(i)$; t' is highest near the mainlobe where the sidelobes are highest. For example, if $\tilde{s}_{can}(i)$ is near the location of the first sidelobe and when $PSNR$ is high (e.g., that seen in Figure 3a), the level of t' is high. The threshold t' is highest when both $\tilde{S}(i;PSNR)$ and $PSNR$ are high. Conversely, at the same range location, however, t' may be negligible when the $PSNR$ is low. C_4 allows the level of $\tilde{s}_{can}(i)$ to be 1 dB lower but within 15 dB of s_{peak}.

There is one free parameter, T, in the calculation of t'. We find that setting T to 3 dB removes the artifacts seen in Figure 3b. There is <1% of the population with $PSNR < 10$ dB, so we only consider those profiles with $PSNR > 10$ dB. The average $PSNR$ of both populations in 2010 and 2011 is ~23 dB (see Figure 3a) and we wanted T to have its maximum effect before the $PSNR$ of the population average is reached; therefore, we selected 20 dB to be that breakpoint. Lastly, since we allow $\tilde{s}_{can}(i)$ to be within 15 dB of the s_{peak}, t' is altered as $\tilde{S}(i;PSNR)$ approaches −15 dB and the $PSNR$-dependent adjustment is added to t' when $\tilde{S}(i;PSNR) > -20$ dB. To avoid the selection of a sidelobe, C_5 selects the peak that is closer to the s-i

interface if there exists a higher candidate peak nearby that is within the expected distance between a mainlobe and a sidelobe in the system response.

3.4. Other Limitations and Considerations

Here, we consider other issues in the determination of snow depth. The finite resolution of the radar imposes a lower limit on detectable snow thickness. Since it takes at least two to three resolution elements to define a peak, we find ~8 cm to be the low limit in snow depth detectability [*Kwok et al*., 2011]. Thus, if the coverage of thin snow were extensive, then biases in the regional averages would be expected.

Assuming a nominal density of 300 kg/m^3 with an expected variability of $\sigma_c = 50$ kg/m^3, the uncertainty in the snow depth estimate varies from ~3.5 to 5 cm for snow depths between 10 and 70 cm [*Kwok et al*., 2011]. In an ideal scenario, the interfaces would be step edges and the peaks would be of comparable magnitude. However, detection of the interfaces is affected by each of the factors mentioned earlier. A more realistic analysis should include the expected variability of the interfaces within a radar footprint. Even though the peak in the s-i interface is distinct, this is not always the case for the a-s interface and thus typically there is higher uncertainty in the retrieval of its location.

Variability in snow density (and grain size and layer structure) may be an issue in the estimation of snow depth. But, if we can assume that the bulk density of the snow volume is a reasonable approximation for calculation of the refractive index, then the snow depth estimates are relatively insensitive to uncertainties in bulk densities of 100 kg/m^3 [*Kwok et al*., 2011]. However, as discussed above, if the vertical structure of the snow layer modifies the scattering significantly, then this variability may need to be considered. This would be a challenge unless these snow properties can be inferred directly from the radar data. Field programs could certainly provide bounds on variability, but the sampling requirements are daunting. Where vertical layering impacts the scattering significantly, the impact would be to reduce the apparent snow depth relative to the true snow depth.

A last potential consideration is seawater flooding and snow ice formation. When the basal snow layer is saturated, the radar cannot penetrate the slush, and the apparent s-i interface would now be seen at the slush surface (the freeboard level), or slightly above if brine wicking were significant [*Massom et al*., 2001]. However in this case, the slush can be considered as contributing to ice draft and not the snow depth. Snow depth is then defined here as the unflooded snow above the freeboard level.

4. Assessment of Retrievals From Repeat Tracks

We assess the retrieved snow depth from two flights in 2011, one on 12 October and the other on 25 October, that repeated a ~3700 km track with east-west crossings of the Weddell Sea (see Figure 5). Both surveys begin at a point just east of the northern tip of the Antarctic Peninsula. From there, the eastbound leg crosses the Weddell Sea (~1500 km) to Cape Norvegia, the second leg then heads southwest hugging the coast before turning west, south of the Brunt Ice Shelf, for the return crossing of the Weddell. These surveys terminate just south of James Ross Island. In this section, we examine the snow depth distributions and their relationship to radar backscatter, surface roughness, and freeboard. Comparison of the results (summarized in Figures 5, 6, and 7) allow for examination of the spatial patterns, consistency, and limitations of the approach.

Throughout this paper, a snow density of 300 kg/m^3 is used to convert the range separation between the two interfaces into snow depth. At this density, the propagation speed is ~0.81 times the speed of light in free space. While this bulk density is slightly lower than the average observed over the Southern Ocean, and particularly for late spring [*Massom et al*., 2001] increasing the density by 100 kg/m^3 changes the speed by only ~5%, so the estimated depth is not particularly sensitive to variations in bulk density. As discussed earlier, inhomogeneities in the snow volume (e.g., internal layers, density variations, etc.) could introduce higher uncertainties into this conversion factor.

4.1. Snow Depth Distribution and Ice Freeboard

Figures 6a, 6b, and 6c shows mapped profiles of snow depth and 2 m air temperatures (color-coded) of the repeat tracks. The air temperature (T_{2m}) serves as a proxy indicator of radar penetration due to snow wetness: above -5°C, penetration into the snow layer may be reduced [*Winebrenner et al*., 1994]; the maps

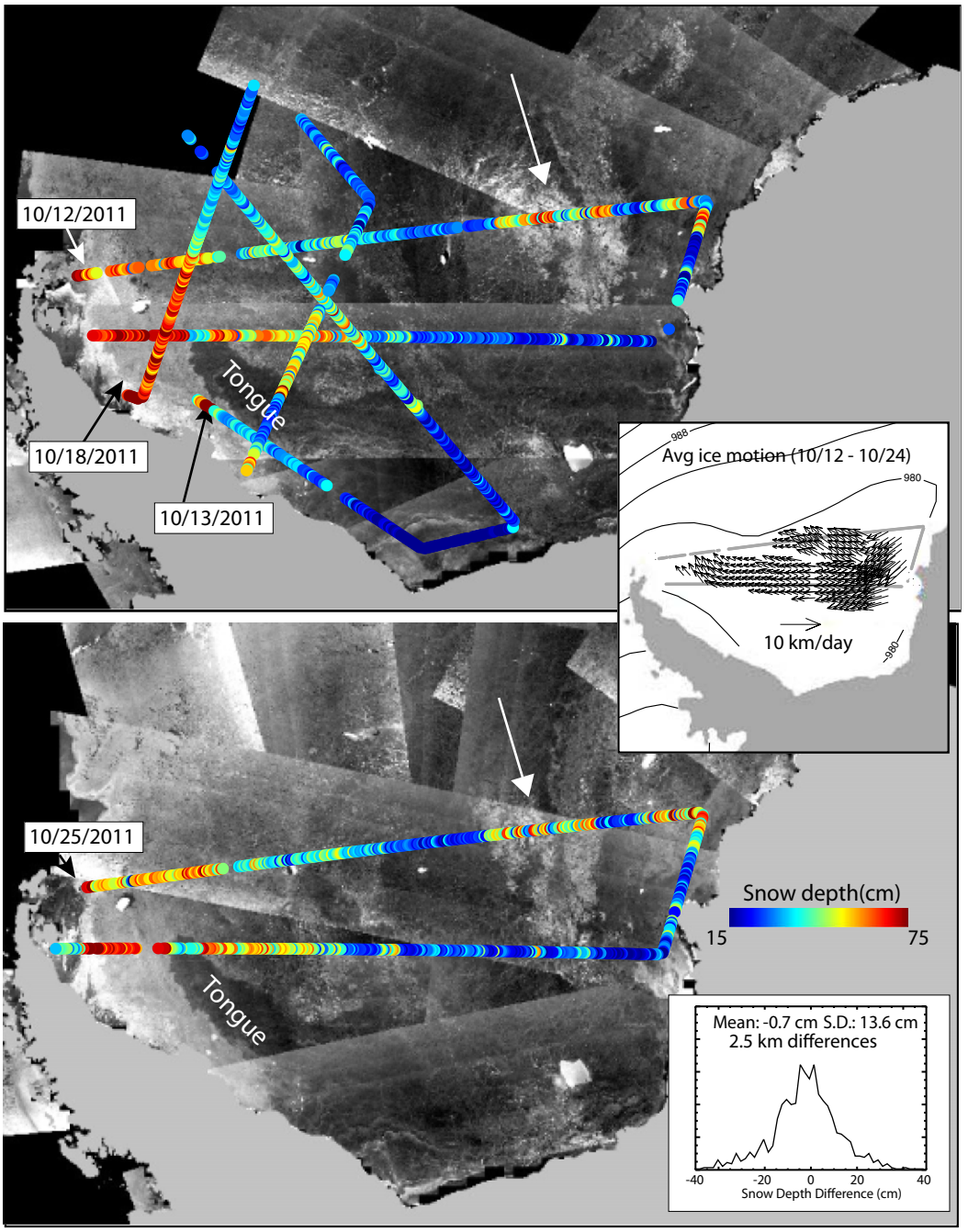

Figure 5. Derived snow depths from the Weddell Sea OIB surveys overlaid on Envisat SAR mosaics. (top) Snow depth from the first 3 days (~4 km averages). Mosaic is constructed using imagery between 10 and 12 October. (bottom) Snow depth from 25 October, a near exact repeat of the track flown on 12 October. Mosaic is constructed using imagery between 25 and 28 October. (top inset) Average ice motion between 12 and 24 October from Envisat SAR imagery and contours are average sea level pressure from ECMWF fields (contour interval: 4 hPa). (bottom inset) Distribution of along-track differences in snow depth between the repeat tracks flown on 12 and 25 October. Differences are from 2.5 km averages.

show T_{2m} that are below $-5°C$ on both days and thus wetness was unlikely an issue in the interpretation of the data. Broadly, a thick snow cover (60–70 cm) is found in the western Weddell near the coast in the repeat tracks (see Figures 6b and 6c, also Figure 5), which then transitions into a region of thinner snow (30–40 cm) over the central Weddell. In the eastern Weddell (at ~1100 km along the track), a region of thicker snow (50–60 cm) is encountered before approaching the coast. South of Cape Norvegia, just off the Riiser-Larsen Ice Shelf, the snow thins to 20–30 cm. On the return tracks in the south, the snow in the

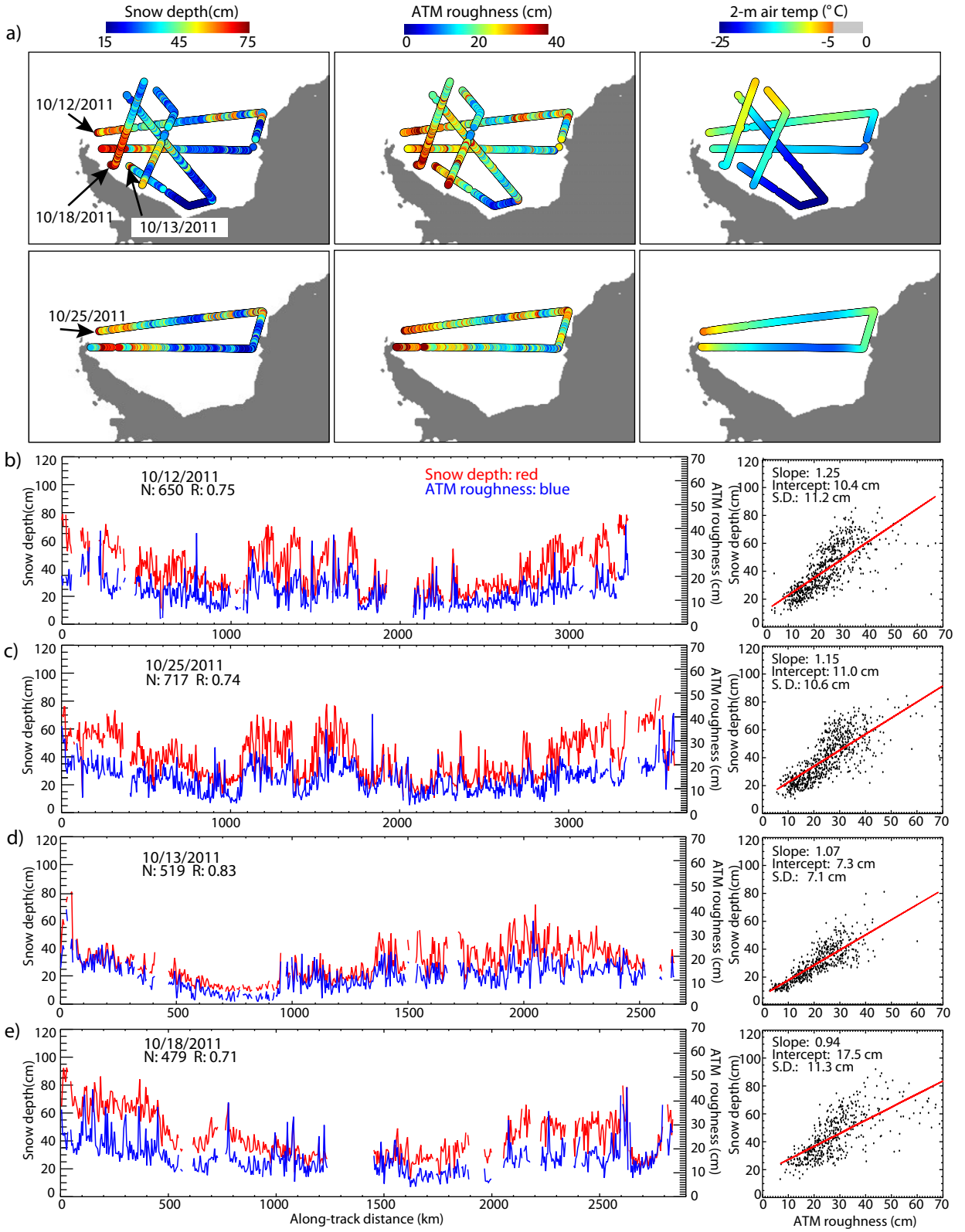

Figure 6. Four Weddell Sea tracks in October of 2011. (a) Profiles of (left) 4 km snow depth, (middle) roughness, and (right) 2 m air temperature. (b) 12 October: (left) Along-track profiles and (right) scatterplot of snow depth and roughness (4 km averages). R is the correlation between the two parameters; Regression slope, intercept, and standard deviation are shown on the scatterplot. (c–e) same as plot (b) but for 25, 13, and 18 October. Roughness is standard deviation of detrended surface elevations from the ATM lidar.

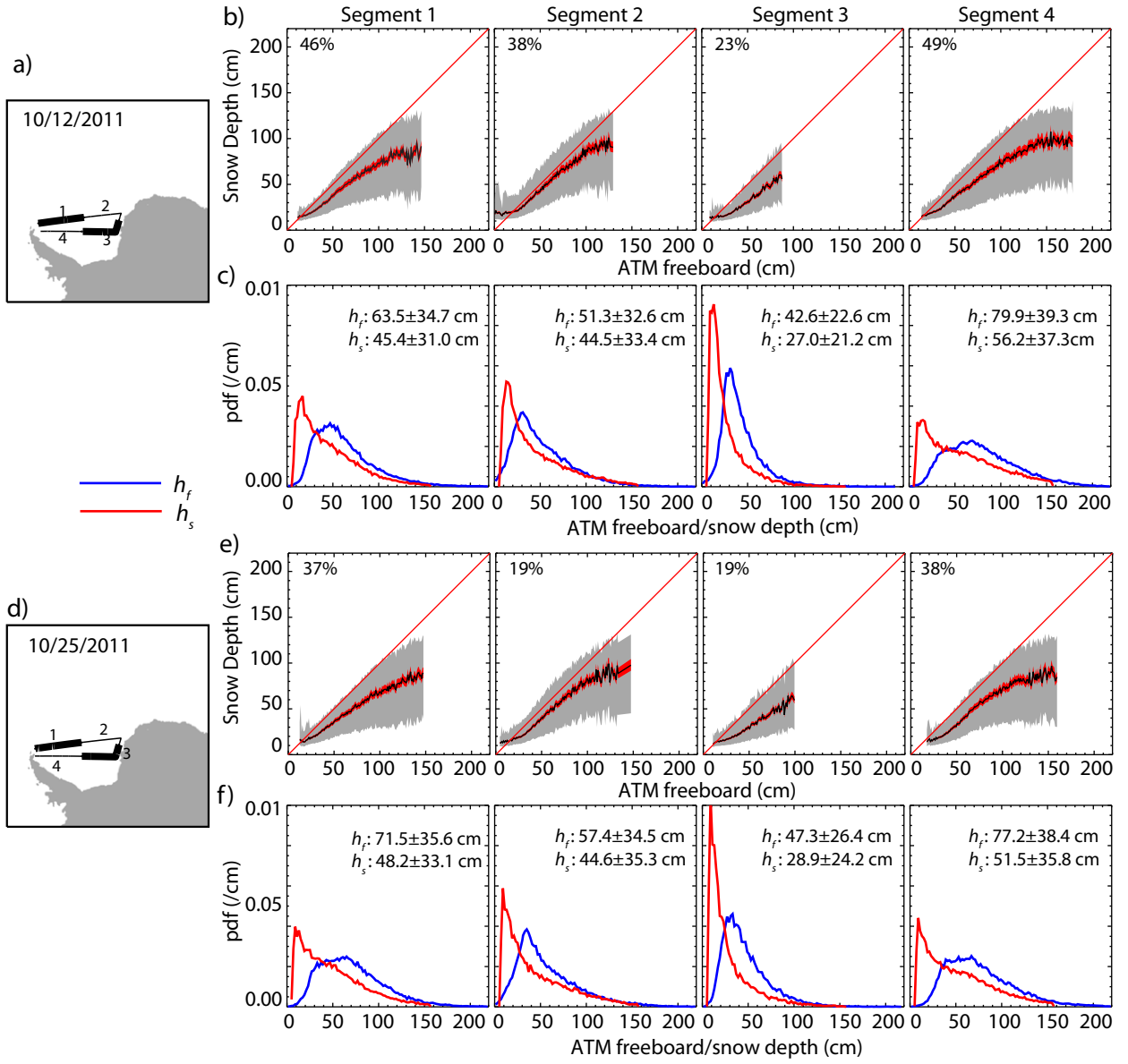

Figure 7. Snow depth and total freeboard (snow + ice) from the 12 and 25 October 2011 surveys. (a, d) Track/segment location. Tracks are divided into four flight segments (of ~700 km in length) for examination of regional statistics. (b, e) Relationship between snow depth (h_s) and total freeboard (h_f) for each segment: the gray bands show the ±RMS excursions within 1 cm bins, and the red band shows the variability associated with an uncertainty in snow density of ±100 kg/m^3. Retrieval percentage is in top left corner (see text). (c, f) Distribution of snow depth and freeboard within each segment along the track. Mean and standard deviation of the distributions of snow depth (h_s) and freeboard (h_f) are shown in each panel. Samples are averages of ATM elevations and snow radar retrievals along ~20 m intervals on the track; this represents six ATM elevation samples (~3 m spacing; 1 m resolution) and three samples from 2011 snow radar retrievals (5 m sample spacing; ~7 m resolution).

eastern Weddell is generally thinner compared to that seen in the eastbound tracks further north. The snow then thickens as the tracks approach the western Weddell and the coast of the Antarctic Peninsula.

The regional distributions in snow depth in four nearly overlapping segments of ~700 km in length can be compared. Figures 7c and 7f show snow depth distributions (in red) of each segment. Except for Segment 4, it can be seen that the shapes of the distributions are similar and the mean snow depths are on average 2 cm of each other. As the tracks do not cover exactly the same distances, we attribute the differences to the inclusion of that stretch of thinner ice at the end of the longer survey on 25 October (see Figures 6b and 6c, also Figure 5). At this length scale, the retrievals seem to be consistent to within several centimeters.

The smaller scale differences between the repeat tracks (seen in the figures) are examined in a following section.

Next, we examine the relationships between snow depth (h_s) and total freeboard (i.e., snow + ice freeboard) in Figure 7. Total freeboard (henceforth referred to as freeboard, h_f) is derived from the ATM lidar elevations using the procedure described by *Kwok et al*. [2012]. Based on one assessment in the Arctic, an average precision of ~4 cm seems achievable [*Kwok et al*., 2012]. In Figures 7b and 7e, snow depths that are greater than the estimated freeboard are above the red line with unity slope, i.e., where freeboard equals snow depth. Even though negative ice freeboards are expected in the Antarctic it is unlikely that the radar would penetrate the high salinity flooded surface and hence we do not expect measurements above the red line. However, since noise contributes to the freeboard as well as the snow depth estimates, it is expected that some fraction of the snow depth estimates will be greater than the total freeboard. When the two estimates are comparable (i.e., ice surface near the sea surface), the population is more evenly distributed on either side of the line. For sea ice with higher ice freeboard, most of the population would reside below the red line.

The snow depth and total freeboard results from different segments in the repeat tracks are remarkably consistent (Figure 7); the relationships between the two estimates and the fraction (or the area) of total samples that are above the red line are comparable. There is a linear relationship between snow depth and freeboards for freeboards below ~100 cm, although in most cases, the snow depth is somewhat less than the total freeboard, i.e., there is a nonzero sea ice freeboard. Another feature (seen in Figures 7b and 7e) is that the snow depth levels off at a certain freeboard beyond which changes in snow depth becomes negligible. Differences in this level in the four segments suggest a regional dependence. If the average net regional precipitation and accumulation of snow places a limit on the maximum snow depth, then the plateau could be an expression of this limit. Here, accumulation includes all the processes that control the regional snow depth, e.g., wind-driven redistribution, flooding and snow-ice transformation, ice age, and ice deformation. This leveling-off is also seen over Arctic sea ice [*Kwok et al*., 2011]. This plateau is highest in Segment 4 of the repeat tracks where we expect the deepest snow over multiyear sea ice. Alternatively, this leveling-off could also be due to a penetration depth limit of the radar. However, regional differences in this level suggest a geophysical explanation is more likely. For example, the highest plateau occurs in the southwestern Bellingshausen Sea (Figure 12b) where we would expect more icy layers and snow wetness than in the Weddell Sea due to greater frequency of warm weather incursions.

Segment 2 stands out as having a consistently higher fraction of the samples above the red line than the others. Possibly, this is an area where negative ice freeboards are prevalent, although negative ice freeboards of more than a few centimeters are very rare without seawater flooding occurring [*Maksym and Jeffries*, 2000], and unlikely to be sustained in spring as the ice warms and sea ice permeability increases. We should also remember that the assumptions of bulk density might introduce variability in retrievals that is not well understood. The different footprints of the snow radar and ATM lidar sampling slightly different spots are another source of variability. Since these parameters are measured independently, systematic biases in the freeboard and snow depth estimates would shift these curves horizontally and vertically without changing the slope.

4.2. Retrieval Rates

Here, we turn our attention to the retrieval rates shown on the top left corners of Figures 7b and 7e. The retrieval rate is the ratio of the number of detected a-s interfaces to the total number of radar returns. For the repeat tracks, the results show that the retrievals are fairly consistent. On both days, the rates are consistently higher (between 37 and 49%) in those segments with thicker snow (Segments 1 and 4) and lower (between 19 and 23%) in those segments with the thinner snow (i.e., Segment 3). We first address the rate of detection and then the impact of this rate on sampling the snow depth distribution.

The radar returns that do not contain candidate peaks that satisfy conditions C_1 through C_5 (discussed in section 3) are removed from consideration. In ~5–20% of the returns, there are no local peaks that satisfy C_1 and C_2. Rejections are higher in the noisier radar data from the 2010 campaign; the published 2011 Antarctic data sets have an additional averaging step that reduces noise in the echograms (discussed in section 2). A larger fraction of the rejections are due to the failure of the candidate peaks to satisfy C_3 and C_4. Approximately, 10–40% of the candidate peaks are not selected by C_3 and of the remaining peaks

Table 2. Mean and Standard Deviation of Freeboard and Snow Depth of Four Segments Along Each Weddell Sea Flightline[a]

Units (cm)	Freeboard (f)			Snow Depth (s)		
Weddell	h_f	h_f'	h_s	h_s'	h_s''	$h_s - h_s''$
26 Oct 2010						
S1	65.4 ± 28.5	61.3 ± 33.8	38.8 ± 25.0	36.7 ± 16.6	37.4 ± 19.7	1.4
S2	45.5 ± 19.9	42.9 ± 23.4	33.1 ± 20.9	31.6 ± 16.1	32.0 ± 17.6	1.1
S3	49.9 ± 27.8	49.3 ± 32.0	27.3 ± 22.9	27.2 ± 15.6	27.2 ± 17.1	0.1
S4	69.1 ± 33.1	65.3 ± 38.5	42.9 ± 29.6	40.8 ± 19.3	41.4 ± 22.5	1.5
28 Oct 2010						
S1	102.2 ± 46.0	96.5 ± 53.2	55.9 ± 38.4	51.7 ± 18.9	53.0 ± 26.3	2.9
S2	64.2 ± 36.5	58.2 ± 38.8	38.1 ± 32.2	33.9 ± 21.6	35.0 ± 24.9	3.1
S3	56.5 ± 27.0	50.7 ± 31.7	41.3 ± 28.8	37.5 ± 21.2	38.6 ± 23.8	2.7
S4	52.9 ± 27.3	48.7 ± 31.5	30.1 ± 21.1	28.4 ± 12.9	28.9 ± 15.9	1.2
13 Oct 2011						
S1	51.7 ± 33.8	35.8 ± 33.8	34.3 ± 30.1	24.7 ± 14.5	26.2 ± 18.3	8.1
S2	43.0 ± 23.2	27.2 ± 20.6	25.4 ± 21.3	17.7 ± 10.2	18.5 ± 12.2	6.9
S3	54.9 ± 30.3	41.1 ± 32.0	39.6 ± 30,6	30.5 ± 22.1	32.7 ± 24.7	6.9
S4	57.0 ± 28.6	48.2 ± 42.0	38,5 ± 27,9	34.7 ± 21.7	35.9 ± 23.9	2.6
18 Oct 2011						
S1	92.5 ± 49.2	80.3 ± 54.4	60.1 ± 38.6	52.2 ± 26.6	54.8 ± 31.2	5.3
S2	59.8 ± 30.5	47.7 ± 35.7	36.9 ± 27.6	30.2 ± 20.0	31.9 ± 22.4	5.0
S3	46.0 ± 24.8	40.3 ± 28.8	33.3 ± 24.1	30.4 ± 18.0	31.2 ± 20.0	2.1
S4	73.3 ± 39.7	61.7 ± 62.3	48.7 ± 35.6	39.7 ± 22.2	41.7 ± 26.1	7.0
12 Oct 2011[b]						
S1	63.5 ± 34.7	54.5 ± 71.2	45.4 ± 31.0	39,2 ± 22.8	41.2 ± 25.9	4.2
S2	51.3 ± 32.6	38.0 ± 51.7	44.5 ± 33.4	35.8 ± 24.4	38.3 ± 27.6	6.2
S3	42.6 ± 22.6	30.4 ± 24.0	27.0 ± 21.2	21.5 ± 15.0	22.5 ± 16.3	4.5
S4	79.9 ± 39.3	70.3 ± 56.6	56.2 ± 37.3	49.2 ± 26.0	51.5 ± 30.4	4.7
25 Oct 2011[b]						
S1	71.5 ± 35.6	55.7 ± 43.1	48.2 ± 33.1	39,3 ± 22.5	41.7 ± 26.0	6.7
S2	57.7 ± 34.5	43.2 ± 48.7	44.6 ± 35.3	34.5 ± 24.5	36.8 ± 27.3	7.8
S3	47.3 ± 26.4	34.4 ± 26.2	28.9 ± 24.2	22.6 ± 15.0	23.5 ± 16.7	5.4
S4	77.2 ± 38.4	66.0 ± 50.6	51.5 ± 35.8	43.3 ± 24.0	45.6 ± 28.0	5.9

[a]See text for a description of the variables.
[b]Repeat tracks.

~10–20% are removed by C_4. Effectively, these conditions determine whether the strength of an a-s return is strong enough under different sidelobe and signal-to-noise conditions to be selected. The dependence of retrieval rate on snow thickness can be attributed to the level and location of the first sidelobe. When the snow is thicker, the a-s returns are away from the effects of the first sidelobe (typically the highest) and thus the retrieval rate is higher. As the snow gets thinner, the a-s returns are closer to the first sidelobe (i.e., thinner snow), and because of C_3 more of the returns are rejected. The effectiveness of the retrieval approach can be seen in the results in Figure 3. Further, when the level of the first sidelobe for a given radar installation is higher (as in 2011, discussed earlier), the negative impact on detection is higher.

Due to the incomplete sampling of the snow depth distribution discussed above, a question is whether our approach would bias the statistics of the distributions due to selective retrievals over certain ice and snow surfaces. One way to address this question is to examine the potential of sampling biases by comparing the total freeboard distributions of samples with snow depth retrievals (h_f in Figure 7) to the distributions of those samples without retrievals (h_f'). The differences are shown in Table 2 (the repeat tracks are shown in the last two rows). Indeed, the results show that there is a selective sampling of the snow cover over sea ice with higher freeboard (i.e., $\bar{h}_f > \bar{h}_f'$). To further quantify this effect on the retrieved snow depth, we use the tabulated relationship between mean snow depth and freeboard (i.e., $h_s = f(h_f)$, defined by the black curves in Figure 7) to estimate the snow depths (h_s') that are not sampled by the retrieval algorithm. With h_s', we can then compute the mean snow depth of the overall distribution (h_s'') for assessing the mean biases $h_s - h_s''$ between the distributions. For these repeat tracks, the biases in the averaged snow depth are between 4.2 and 7.8 cm, largely due the undersampling of thin snow—a limitation due to the resolution of the snow radar and undersampling of the snow cover.

It is also possible the observed freeboard-snow depth relationships do not hold for the missing retrievals. For example, ice with very little snow (below the detection threshold) would not obey this relationship, and

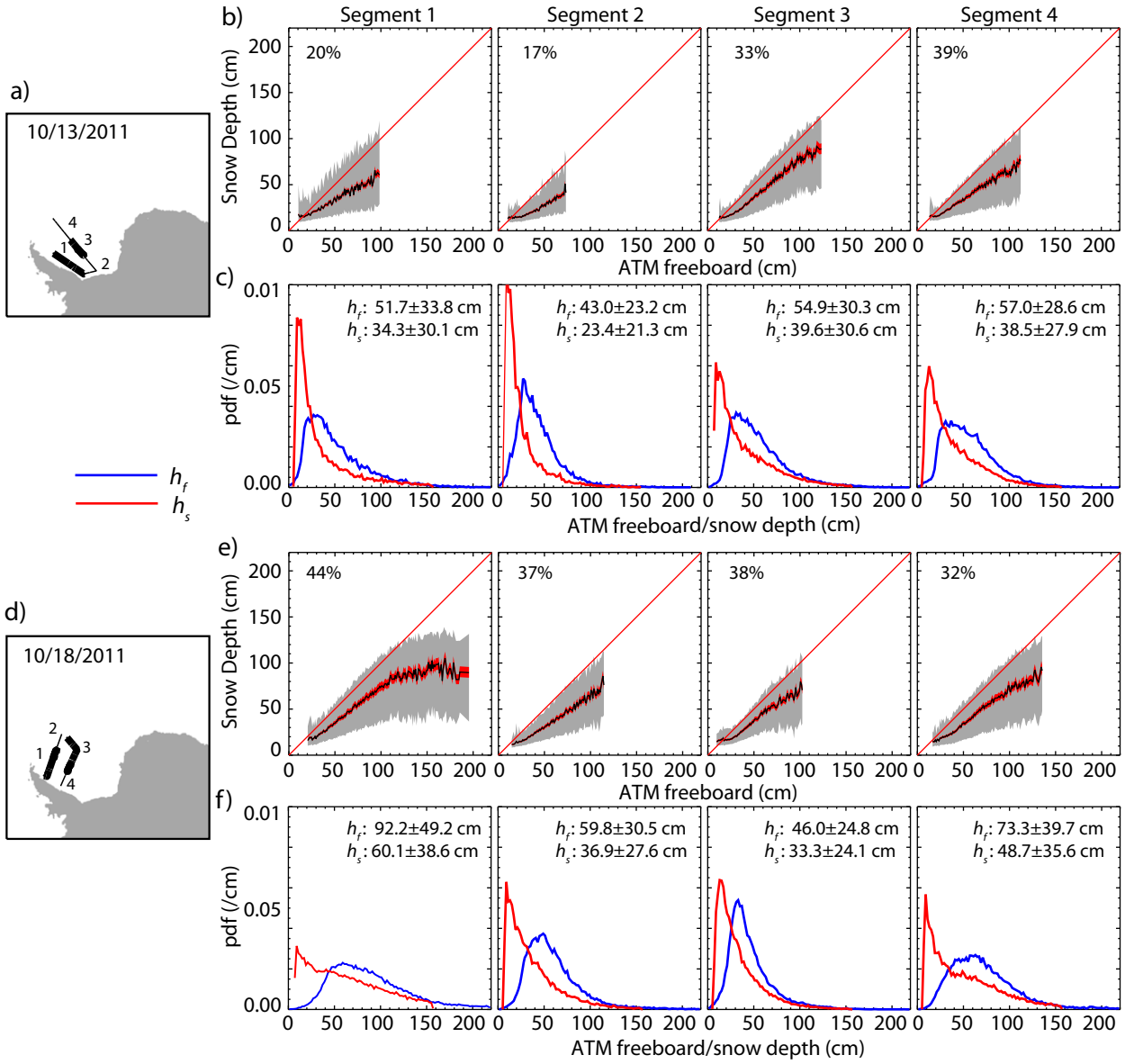

Figure 8. Snow depth and total freeboard (snow + ice) from the 13 and 18 October 2011 surveys. Caption as in Figure 7.

the slope would fall below the unity line in Figures 7b and 7e. This may occur in Segment 2 in the 13 October 2011 survey (Figure 8b), where the OIB flightline flew over areas of young ice with less snow in front of the Ronne Ice shelf, with the lowest observed retrieval rate. Generally, retrieval rates tend to be lower over areas of thin snow. This would increase the positive bias in the OIB data as an estimate of the areal averaged snow depth.

As can be seen in Table 2, the biases are noticeably lower in the 2010 retrievals. We attribute this to the sidelobe structure of the 2011 radar returns. The level of the first sidelobe located at ~30 cm in radar range (or, 24 cm after conversion to snow depth) in the 2011 radar returns is 3–4 dB higher than the first sidelobe at around the same location in the 2010 returns (see Figure 3). Thus, the strength of the returns from the a-s interfaces has to be much stronger than that of the sidelobe to be selected as a valid geophysical return. In effect, this reduces the retrievals in the 25–35 cm radar range (or, 20–28 cm after conversion to snow depth). And, this could cause a significant undersampling of the snow depth distribution below 30 cm. On the other hand, if one were to mistakenly sample the radar sidelobes at this location, the contribution could have a detrimental effect on the shape of the distribution (as illustrated earlier).

4.3. Snow Depth, Radar Backscatter, and Ice Motion

The along track variability in snow depth can be compared to the spatial pattern in radar backscatter in 3 day mosaics of Envisat SAR imagery around the two flight days (see Figure 5). Snow is the thickest in that area of distinctly higher backscatter in the northwestern Weddell Sea off the east coast of the Antarctic Peninsula. In contrast, that tongue of lower backscatter ice that extends from the southern Weddell into this area of high backscatter has a snow cover that is 20–30 cm thinner (see also along-track profiles in Figure 6). These observations suggest that thicker snow is associated with areas of higher radar backscatter, thought to be generally indicative of a rougher surface or multiyear ice. The tongue of low backscatter ice is associated with first-year ice that has formed in the Southern Weddell Sea adjacent to the Ronne ice shelf and drifted north. This is a region of particularly low snowfall [e.g., *Giovinetto and Bentley*, 1985; *Maksym and Markus*, 2008]. Multiyear ice in the Weddell Sea is well known to possess deep snow cover [e.g., *Massom et al*., 1997]. Rougher, deformed areas are known to be catchments for deeper snow [*Worby et al*., 2008a]. Other areas showing such associations between backscatter and snow depth can be found by inspection of Figure 5.

Further, differences in snow thickness between the 2 days can be partially explained by advection of spatial patterns in radar backscatter due to ice motion. Available 12 day motion field from Envisat (shown as an inset in Figure 5) show northward motion in the western Weddell, westward motion in the central Weddell, and southward motion in the eastern Weddell. In the ∼12 days between the two SAR mosaics, the tongue of lower backscatter ice that extends from the southern Weddell (discussed above) has moved northward increasing the width of the tongue sampled by the repeat track on 25 October. This can be seen in the wider segment of thinner snow cover sampled by the flight track on the later day. Another area where changes in snow thickness due to advection can be seen is the southward movement of a patch of sea ice with higher radar backscatter in the northeastern Weddell (see arrows Figure 5). The eastbound leg on 12 October surveyed that patch of sea ice with higher radar backscatter/thicker snow cover in the eastern Weddell, but this patch of ice was not sampled by the return leg in the south. On 25 October, 12 days later, the ice had moved south and the eastbound track in the north is now sampling a different part of that area of higher backscatter. On that day, the return leg sampled the southern tip of that patch of higher radar backscatter, with a higher snow cover, that has moved into the track. Again, this seems to be consistent with the association of snow thickness and radar backscatter. Without accounting for the impact of ice motion, the mean difference in snow depth (2.5 km averages) between the two tracks is −0.7 cm (standard deviation: 13.6 cm). 25 October is slightly thinner. However, it seems from this discussion that even though the spatial patterns are consistent, that ice motion induced effects may be a significant contributor to the observed local variability between the 2 days.

4.4. Snow Depth and ATM Surface Roughness

We found interesting correlations between mean snow depth and surface roughness. We define roughness as the standard deviation of detrended surface elevations from the ATM lidar. The profile of the two estimates (calculated at 4 km length scales) and their scatterplots can be seen in the two plots in Figures 6b and 6c. Correlations between snow depth and surface roughness are 0.75 and 0.74 for 12 October and 25 October, respectively. Linear regression gives slopes of 1.25 and 1.15 with intercepts of ∼11 cm. This suggests that snow tends to collect in rougher areas perhaps due to wind redistribution. This is consistent with the fact that deformed ice tends to trap deeper snow [e.g., *Worby et al*., 2008a; *Markus et al*., 2011]. This also shows consistency in the retrievals when examined with independent data from the lidar.

5. Snow Depth Results

In this section, we examine the retrievals from four additional OIB snow radar tracks over the Weddell Sea (two each from October of 2010 and 2011) and two tracks from the Bellingshausen Sea (one from October of 2010 and 2011). Using the same methods as in the analysis of the repeat tracks in the previous section, we describe the interannual differences and spatial patterns seen in the remaining OIB tracks as an example of the efficacy of the method for detecting spatial and temporal variability in snow depth distribution. As such, our goal here is not to examine the geophysical phenomena driving such variability; that is reserved for subsequent studies.

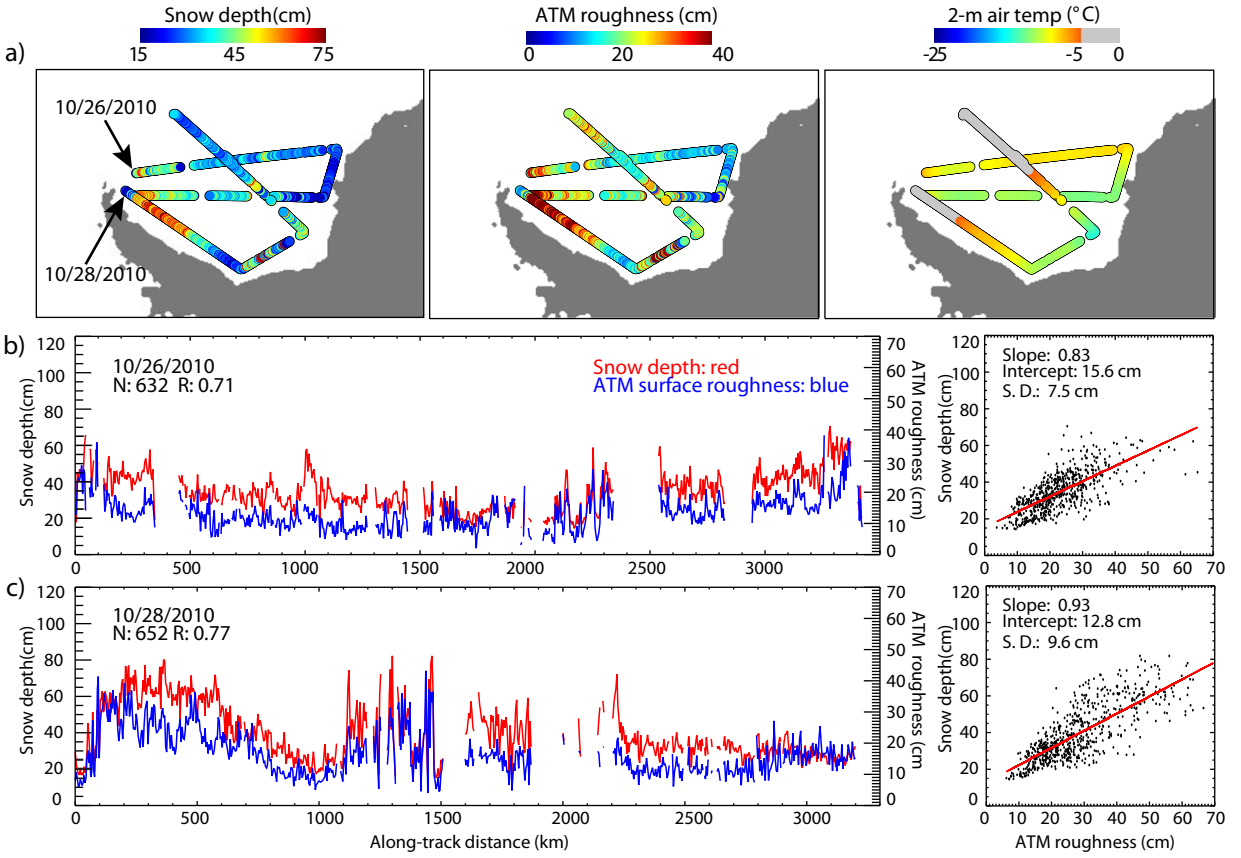

Figure 9. Two Weddell Sea tracks in October of 2010. Caption as in Figure 6.

5.1. Weddell Sea:26 and 28 October 2010

The flight on 26 October acquired data over the repeat tracks discussed in section 4: an approximately 3700 km track with return crossings of the Weddell Sea (Figure 9). This allows an examination of the interannual variability between 2010 and 2011. Air temperatures (T_{2m}) are below $-5°C$ along the entire track but warmer than that encountered during the 2011 flights. The track started further east compared to the tracks on 2011 (Figure 6b) and has a lower snow depth than that found in Figure 6b. There is a more gradual transition from the thicker snow cover (40–50 cm) in the western Weddell into a region of thinner snow (30–40 cm) over the eastern Weddell. There is no evidence of that patch of thicker ice in the eastern Weddell in 2011 (discussed in the previous section). Similar to that observed in the return leg in October 2011, the snow in the eastern Weddell is generally thinner compared to that seen in the eastbound track further north. The snow becomes gradually thicker as the track approaches the western Weddell and the coast of the Antarctic Peninsula. The east-west gradients in snow depth are lower in 2010.

The retrieval rates for 2010 (in Figure 10b) are comparable to those in 2011. Similar to 2011, the rates are consistently higher (ranges from 36 to 42%) in those segments with thicker snow (Segments 1 and 4) and lower in segment 3 (∼22%) with the thinner snow. The lower biases (0.1–3.1 cm, see Table 2), in the 2010 retrievals can be compared to those in 2011 (2.6–8.1 cm). We attribute this to the lower sidelobes in the radar response (see Figure 3). After adjusting for the biases, the overall differences in the mean snow depth (h_s'') between the repeating tracks in 2010 and 2011 is reduced to $<$10 cm (see Table 3).

Compared to the repeat tracks in 2011 (see Figures 7b and 7e), snow depth is generally thinner in 2010, with a greater difference between snow depth and total freeboard (Figure 10b). The leveling-off or the plateau in snow depth at high freeboards occurs at a lower snow depth, again suggesting that this may be an upper bound of the average net regional precipitation and accumulation. Correlations between the mean snow depth and surface roughness are 0.71 (see Figure 9). Linear regression gives a slope of 0.83, lower

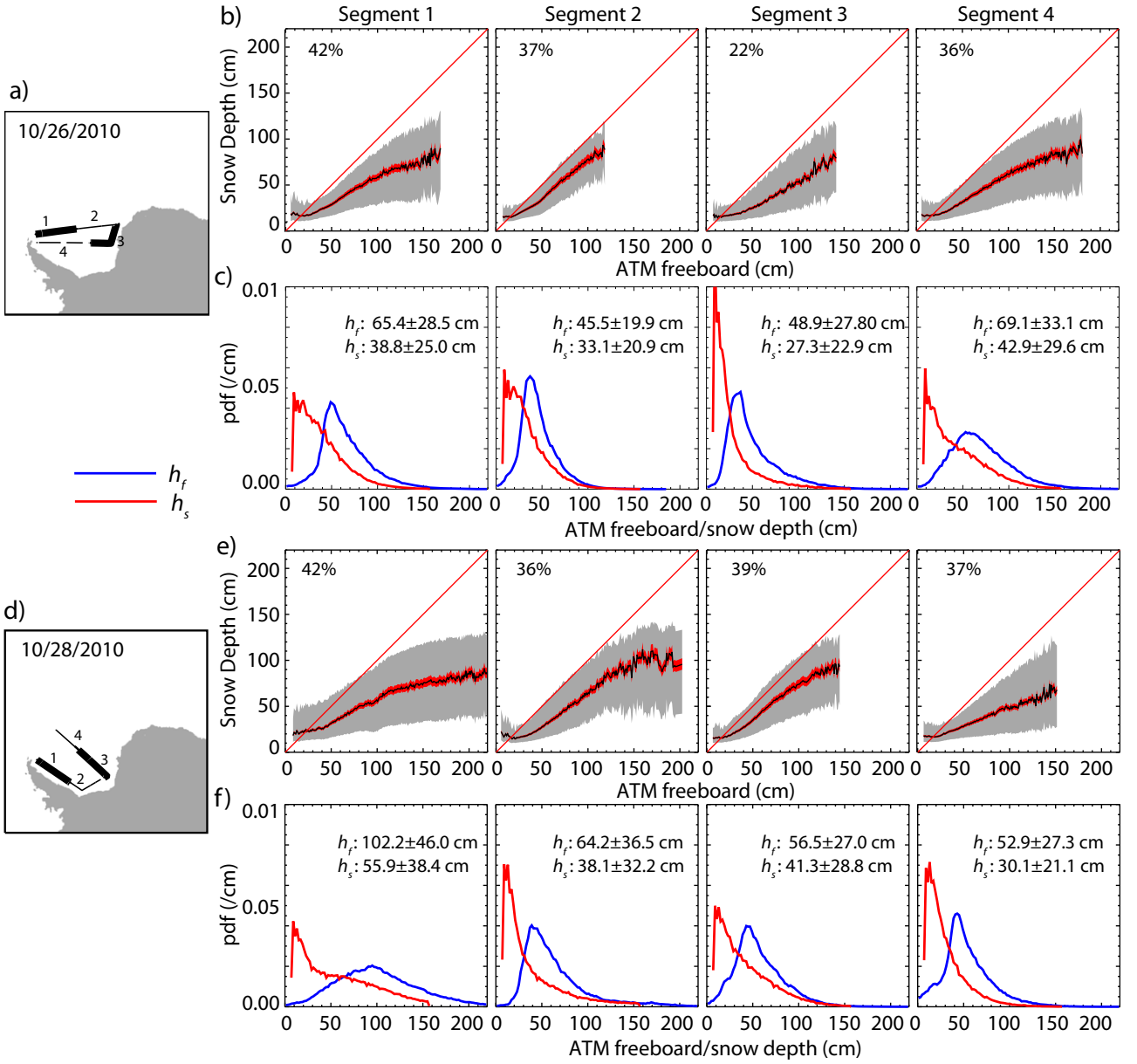

Figure 10. Snow depth and total freeboard (snow + ice) from the 26 and 28 October 2010 surveys. Caption as in Figure 7. Samples are averages of ATM elevations and snow radar retrievals along ~20 m intervals on the track; this represents six ATM elevation samples (~3 m spacing; 1 m resolution) and 15 samples from 2010 snow radar retrievals (1 m sample spacing; ~7 m resolution).

than those seen in 2011 (see Figure 6); although this is also consistent with the expectation that snow tends to collect in rougher areas. Measurements are required to support this interpretation.

The southbound leg on 28 October (Figure 9a) parallels the east coast of the Antarctic Peninsula for ~1000 km, turns east for an ~700 km track that roughly parallels the Ronne Ice Shelf, and then north for a leg of ~1500 km to the ice edge. As a cautionary note, the air temperature was above −5°C north of ~70°S during this flight. There is an area of thinner ice and freeboard (~20 cm) near the tip of the Peninsula that is perhaps associated with thinner ice produced in the Larsen polynya. South of that, the snow depth peaks (70–80 cm) at around 300 km along the track, then thins to ~20–30 cm just before the eastbound leg, where rougher ice and higher snow depth associated with predominantly multiyear ice are encountered. The snow depth in the northbound leg thins to approximately 20 cm at the end of the track.

Table 3. Corrected Snow Depths Statistics (Mean and Standard Deviation) for the 2010 and 2011 Repeat Tracks in the Weddell Sea

h_s''	10/26/10	10/12/11	10/25/11
S1	37.4 ± 19.7	41.2 ± 25.9	41.7 ± 26.0
S2	32.0 ± 17.6	38.3 ± 27.6	36.8 ± 27.3
S3	27.2 ± 17.1	22.5 ± 16.3	23.5 ± 16.7
S4	41.4 ± 22.5	51.5 ± 30.4	45.6 ± 28.0

The retrieval rates are between 36 and 42% (Figure 10e). The lower biases between 1.2 and 3.1 cm (Table 2), compared to those in the 2011 retrievals, are again consistent with our attribution to sidelobes. The plateau in snow depth at high freeboards is lower than in 2011, and consistent with those extremely deep snow depths on 26 October. Correlations between the mean snow depth and surface roughness are 0.77. Linear regression of the two parameters gives a slope of 0.93, compared to 0.83 from the flight on 26 October.

5.2. Weddell Sea: 13 and 18 October 2011

For both flights, the along track variability in snow depth can be compared to the spatial pattern in radar backscatter in 3 day mosaics of Envisat SAR imagery close to the two flight days (see Figure 5).

The track of the flight on 13 October is similar to that of 28 October 2010: starting further south, the first leg in Figure 6a parallels the east coast of the Antarctic Peninsula for ∼600 km, turns east for an ∼300 km track that roughly parallels the Ronne Ice Shelf, and then north for a leg of ∼1500 km to the ice edge—providing a survey of the ice cover of the central Weddell Sea. The thick snow cover (70–80 cm) in the first 100 km of the track is associated with an area of high radar backscatter (see Figure 5). Past this area, there is a sharp drop in snow depth after encountering that tongue of sea ice with lower radar backscatters that extends from the southern Weddell (also surveyed in other tracks). At the south end of this track, the snow cover is <20 cm thick and likely to be associated with thinner ice that is produced by the Ronne Polynya (see also along-track profiles in Figure 6). The snow cover in the northbound leg is more variable: the snow cover peaked at ∼40–50 cm at around 2100 km (higher radar backscatter) along the track before thinning to ∼30 cm before the termination of the flight. Retrieval rates are between 17 and 39% (Figure 8b). As expected and discussed above, the biases due to sampling biases, between 2.6 and 8.1 cm (Table 2), are higher compared to that seen in the 2010 retrievals. In this case, correlation between the mean snow depth and surface roughness at 0.83 is the highest for the Weddell.

Starting at around 67°S, the 18 October track (Figure 6a) heads northeast for ∼1200 km toward the ice edge before turning south. After ∼600 km, the track turns southwest for the return leg to the Antarctic Peninsula. Consistent with the three other surveys in 2011, we find a thick snow cover (70–80 cm) associated with an area of high radar backscatter (see Figure 5) just off the coast of the Peninsula. A decline in snow depth at ∼600 km is associated with a slow transition to lower radar backscatter. In the return leg, the snow gets thicker but drops sharply as the track crosses that tongue of low radar backscatter sea ice described earlier. Retrieval rates are between 32 and 44% (Figure 8e). As expected, the sampling biases between 2.1 and 7.0 cm (Table 2) are higher compared to that seen in 2010 retrievals. In this case, correlations between the mean snow depth and surface roughness are 0.71.

Overall, the results in Figures 5 and 6 show consistency in spatial patterns in the snow depth maps, the correlation to radar backscatter, and the relationships between snow depth, freeboard, and roughness.

5.3. Bellingshausen Sea: October 2010 and 2011

The two flights, one on 30 October 2010 and the other on 23 October 2011, provide repeat tracks for examining interannual variability (Figure 11). The one in 2010 contains only a short data span in the seaward portion of the track. The poleward track (for both flights) surveyed the coastal sea ice from Cape Byrd on the west coast of the Antarctic Peninsula to Pine Island Bay. On both flights, the thickest snow (up to a meter) is found offshore of the Abbot Ice Shelf as well as the tracks within Pine Island Bay. This spatial pattern stands out during both surveys.

Snow depths for most segments (Figure 11) are comparable to those seen in the Weddell Sea, except for the thicker snow offshore of the Abbot Ice Shelf and in Pine Island Bay (segments 2 and 3 in 2010, and segment 2 in 2011). With mean snow depth in these segments of 60–80 cm, these are amongst the deepest snow depths observed. However, they are somewhat comparable to the snow depths observed on Weddell

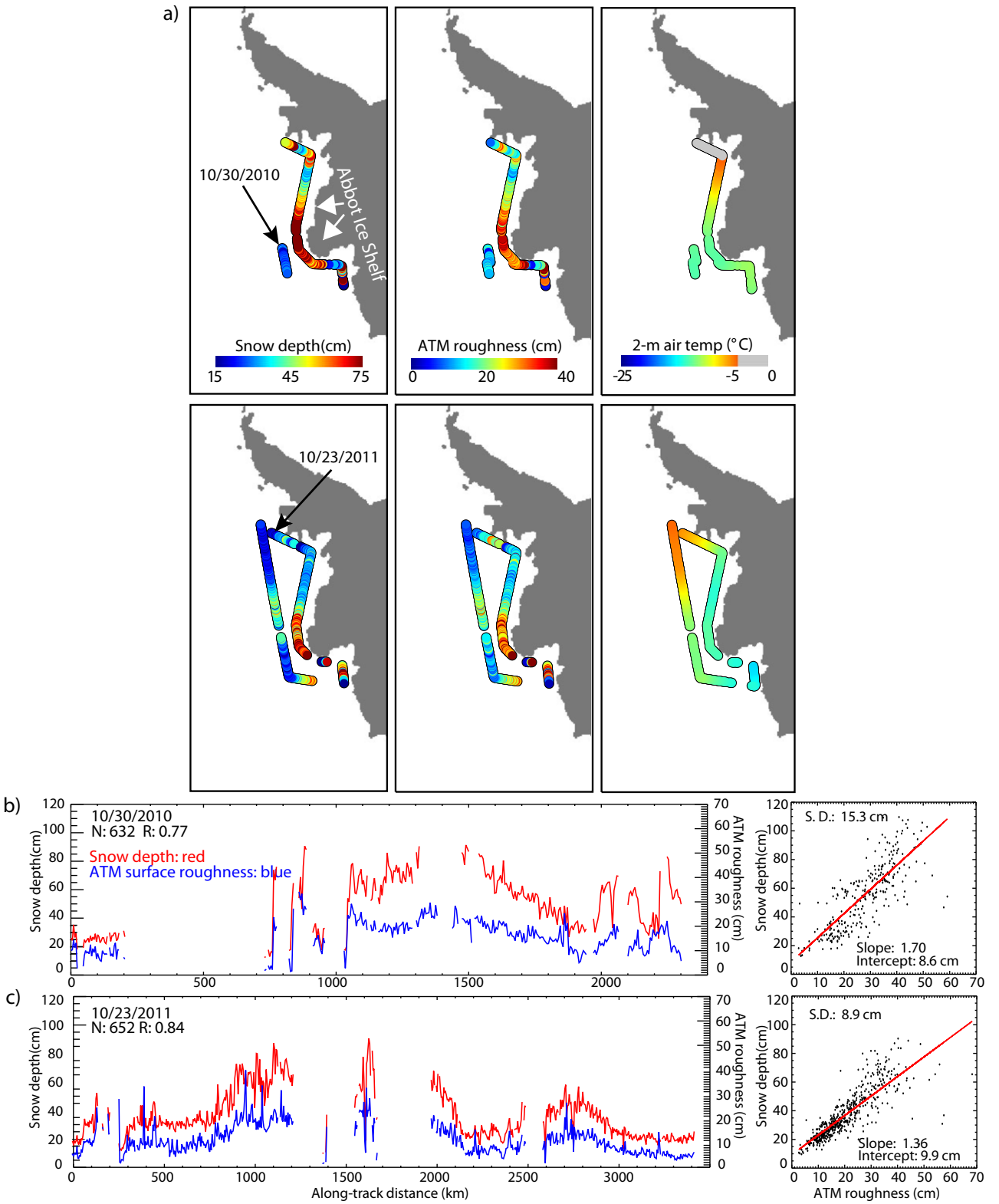

Figure 11. Bellingshausen Sea tracks in October of 2010 and 2011. Caption as in Figure 6.

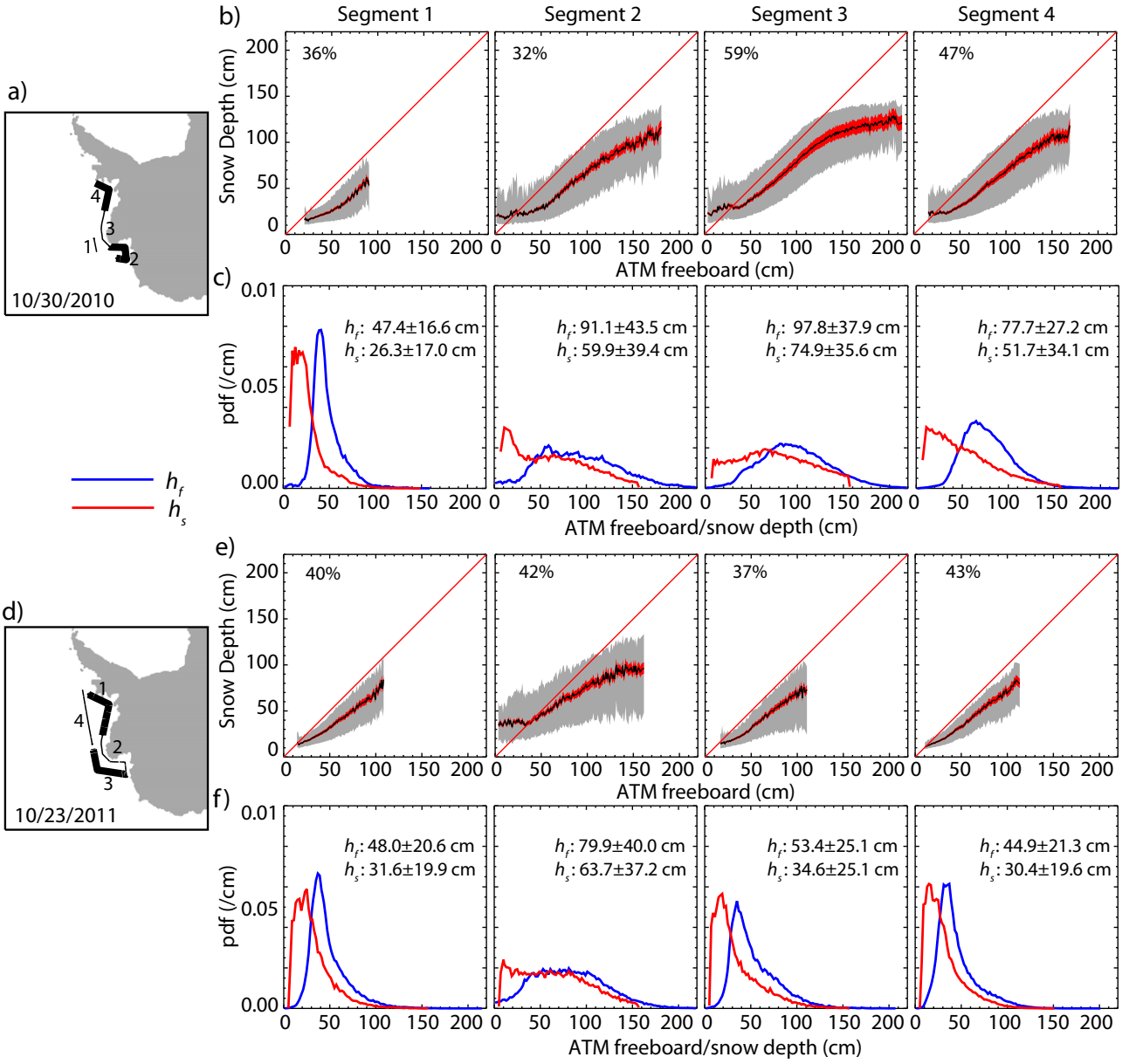

Figure 12. Snow depth and total freeboard (snow + ice) from the 30 October 2010 to 18 October 2011 surveys. Caption as in Figure 7. See Figures 7 and 10 for information on sample population.

Sea segments where multiyear ice is predominant (i.e., segments 1 and 4 in Figure 7, and segment 1 in Figure 8a). Retrieval rates are between 32 and 59% (Figure 12).

The sampling biases are between −0.2 and 9.5 cm (Table 4) for both days. There is less distinction between the 2 days possibly because of reduced sensitivity to the sidelobes because of the thicker snow cover. In this case, correlations between the mean snow depth and surface roughness are 0.77 and 0.84, which are comparable to that observed in the Weddell.

6. Discussion

In this section, we compare these results with available field observations and highlight the proxies of snow depth that we examined in section 5 that are of geophysical interest.

Table 4. Mean and Standard Deviation of Freeboard and Snow Depth at Four Segments Along Each Bellingshausen Sea Flightline[a]

Units (cm)	Freeboard (f)		Snow Depth (s)			
Bellingshausen	h_f	h_s'	h_s	h_s	h_s''	$h_s - h_s''$
30 Oct 2010						
S1	47.4 ± 16.6	46.0 ± 20.2	26.3 ± 17.0	26.6 ± 12.2	26.5 ± 13.7	−0.2
S2	91.1 ± 43.5	71.2 ± 49.2	59.9 ± 39.4	47.2 ± 28.8	50.4 ± 32.3	9.5
S3	97.8 ± 37.9	95.1 ± 44.8	74.9 ± 35.6	72.6 ± 28.7	73.5 ± 32.8	1.4
S4	77.7 ± 27.2	75.6 ± 30.0	51.7 ± 34.1	50.5 ± 20.7	50.9 ± 25.7	0.8
23 Oct 2011						
S1	48.0 ± 20.6	47.6 ± 40.3	31.6 ± 19.9	31.3 ± 15.6	31.3 ± 17.4	0.3
S2	79.9 ± 40.0	77.7 ± 98.2	63.7 ± 37.2	62.0 ± 22.6	62.5 ± 28.1	1.2
S3	53.4 ± 25.1	44.2 ± 30.8	34.6 ± 25.1	30.7 ± 17.3	31.2 ± 19.8	3.4
S4	44.9 ± 21.3	39.9 ± 30.4	30.4 ± 19.6	27.4 ± 16.5	28.3 ± 17.6	2.1

[a]See text for a description of the variables.

6.1. Comparison With In Situ Measurements

The snow depths (and ATM freeboards) are in most cases significantly larger when compared with limited measurements from the field observations. However, it is important to note that the sea ice cover sampled by the OIB tracks has rarely been investigated this late in the season, in part because the depth of penetration possible by ships is limited by thick ice and snow. By mid to late October, the ice cover would have experienced the full season of growth, deformation, and snow accumulation.

Field observations of snow depth distribution are primarily from two sources—underway shipboard observations made while traversing the pack ice (ASPeCt database) [*Worby et al*., 2008b], and mechanical drilling (or snow depth) profiles [e.g., *Massom et al*., 2001]. The overall mean snow depth in the ASPeCt data is 16 cm (all seasons and locations—from 83 voyages and two helicopter flights for the period 1980–2005), less than half the mean snow depth in the present data. Comparing similar regions and seasons, the difference improves somewhat, but there is still a wide discrepancy—in spring, the mean observed snow depth is 24 cm in the western Weddell Sea, and only 17 cm in the Bellingshausen/Amundsen Sea.

There are several reasons these data are not comparable. First, the ASPeCt data include very thin ice types, which are likely not included in the present data set. Distributions of snow depth from the ASPeCt data show the modal thickness is generally in the 0–10 cm range [*Worby et al*., 2008b]—the range that is not sampled by the current retrievals. Second, few of the ASPeCt data have been collected at a similar time and location; indeed, no ASPeCt observations exist for the coastal southern Bellingshausen and Amundsen Seas in spring. Third, the ASPeCt observations are biased toward snow depth over level ice; no correction is made in the data to snow depth for ice deformation as it is for ice thickness. The snow radar retrievals, and prior observations [e.g., *Worby et al*., 2008a], suggest thicker snow is associated with deformed ice areas.

Drilling and snow depth transects may be more comparable data, as they provide a direct measure of snow depth distribution and samples only ice thick enough to stand on—which places a similar cutoff imposed here by the exclusion of very thin ice in the snow radar estimates. However, almost all drilling data to date are from floes thinner than 3 m [*Ozsoy-Cicek et al*., 2013]; the thickest ice (and hence deepest snow) is often avoided. Relatively few snow depth transects have been obtained on multiyear ice. In the Weddell Sea, snow depths have been recorded on several spring cruises [e.g., *Eicken et al*., 1994; *Haas et al*., 2008, 2011]. *Eicken et al*. [1994] describe measurements taken on the Winter Weddell Gyre study in September/October 1989, which traversed the Weddell seaward of the OIB segments 1 and 2 in Figures 7 and 10a. The mean snow depth from the in situ data was 26 cm (compared to 33–48 cm in the OIB data, or ∼32–39 cm after corrected for sample bias), but *Eicken et al*. [1994] also indicate snow depths for heavily deformed and multiyear ice types of 63 and 79 cm, respectively. It is probable that the OIB data contain a greater percentage of these ice types. The in situ snow depths for these ice types are comparable to the OIB estimates for the observed areas of increased SAR backscatter described above. A mean snow depth of 35 cm was reported for transects in the northwestern Weddell Sea in spring on the WWOS cruise in 2006 [*Haas et al*., 2011]. This is 10–20 cm less than the radar-derived snow depth for the OIB segments in this region. Greater snow depths (∼75 cm) were observed on second year ice in late spring in the northwest Weddell Sea on the

2004 ISPOL cruise [*Haas et al*., 2008; *Nicolaus et al*., 2009], comparable or even greater than the OIB snow depth segments in this region, although snow depth on first year ice floes in the vicinity of ISPOL was much less (20–50 cm). The in situ snow depths for first year ice compare well with the modal snow depths observed in the radar data (Figures 7, 8, and 10).

In the southern Bellingshausen/Amundsen, mean snow depths of 23 cm [*Worby et al*., 1996] and 29 cm have been observed in spring [*Jeffries et al*., 1998; *Sturm et al*., 1998]. More recently, snow depths averaging between 10 and 70 cm were observed at several sites in the Bellingshausen in September–October [*Lewis et al*., 2011]. All these measurements were made in the outer pack. These data are thinner ($\sim$5–10 cm), but somewhat comparable to our radar estimates for those segments not immediately adjacent to the coast, particularly if corrected for a possible sampling bias of 5–8 cm discussed in section 4.2. For most coastal segments, our snow depth estimates range between 52 and 78 cm. These are much higher than almost all other snow depth observations anywhere.

As discussed above, the source of the differences between the OIB snow depths and field observation is in large part due to the lack of observations in spring in much of the study areas. In November 2010, the Ice-Bell cruise measured snow depths and ice thickness of selected floes along the coast of Alexander Island [*Williams et al*., 2013] in the vicinity of segment 4 (Figure 12a). Snow probe data from these floes give a mean snow depth of 80 cm above the flooded layer (T. Maksym, unpublished data, 2014), which is actually deeper than the 52 cm mean for this segment, probably in part due to less thin ice in the in situ sample. Snow depths measured in other coastal areas in spring include mean snow depths of $\sim$30 cm on the Antarctic Remote Ice Sensing Experiment (ARISE) in 2003 [*Worby et al*., 2008b], and $\sim$50 cm on the second Sea Ice Processes and Ecosystems Experiment (SIPEX-II) in 2012 (T. Maksym, unpublished data, 2014), both in the east Antarctic sector, which are comparable to the data presented here. Possible reasons for the extreme snow depths seen in some OIB flight segments are discussed in the next section.

6.2. Snow Depth Distribution and Ice Freeboard

Although limited by uncertainties in the estimates of snow depth and freeboard, the relationships between snow depth and total freeboard (i.e., snow + ice freeboard) are useful for contrasting the size of the population with nearly zero ice freeboard with that population with significant ice freeboard. In the plots of snow depth versus total freeboard (Figures 7, 8, 10, and 12), samples with snow depths that are nearly the same as the total estimated freeboard are near the line with unity slope (in red) while samples below the line are those with positive ice freeboard. In all, the average of the distributions (black lines) is below the red line. Deviations from the line are highest when the freeboards are high, especially those in the western Weddell Sea, where thicker ice is expected. Typically, when the freeboards are low (below 40–50 cm), the mean snow depths are just below the total freeboard.

A feature seen in some of the results (see Figures 7, 8, 10, and 12) is that the snow depth levels off or plateaus at a certain freeboard beyond which changes in snow depth become much smaller. Further, this level of snow depths varies with region and seasonally. If the net regional precipitation and accumulation of snow places an upper limit on the maximum snow depth, then the plateau could be an expression of this limit. *Kwok et al*. [2011] also noted this leveling-off over Arctic sea ice. In the Bellingshausen Sea in 2010, this approaches 1.5 m in that track that is close to the Abbot Ice Shelf.

Antarctic sea ice freeboards in field observations usually have means very near zero [e.g., *Maksym and Markus*, 2008; *Ozsoy-Cicek et al*., 2013]. This observation has been exploited by *Kurtz and Markus* [2012] to determine ice thickness from ICESat retrievals of total freeboard. In the freeboard range typical of most field observations (i.e., $<\sim$30 cm), this may be a reasonable assumption. However, the data presented here suggest that for larger freeboards (presumably either heavily deformed ice or multiyear ice), the total freeboard is significantly larger than the snow depth, and hence, the sea ice freeboard is significant. Overall, the mean total freeboards in these data are $\sim$10–30 cm greater than the snow depth, despite deep snow cover. These data suggest that the snow depth and sea ice thickness in the late spring in much of the Weddell, Amundsen, and Bellingshausen Seas may be significantly greater than previously thought. While the bias of 5–8 cm in snow depth due to undersampling of thinner snow reduces the snow depths in many areas to values closer to those seen in field observations, correcting for this bias would actually suggest even thicker ice (due to commensurately greater sea ice freeboard).

It is important to point out areas with much of the snow depths and freeboards presented here would be largely impenetrable to most icebreakers.

As described in the previous section, the snow depths reported here are generally higher than the vast majority of those reported from in situ data. Some of the reasons are described above, but we believe these data suggest that much of the region in the interior pack in spring, particularly near the coast, has much deeper snow (and, by inference, thicker ice) than has been typically described elsewhere [e.g., *Massom et al*., 2001; *Worby et al*. 2008b]. The regions of heavy deformation and multiyear ice in the western Weddell Sea are undersampled (particularly in spring), and these ice types are well known to possess deep snow covers.

Along the southern Bellingshausen and Amundsen Sea coasts, there have been almost no observations. Anecdotal evidence for very deep snow covers in nearby areas is provided by the few ice cores taken in summer in this region—for example, *Jeffries et al*. [1994] report snow depths at coring sites up to 2 m deep on ice up to 7–8 m thick. These represent ice that was thick enough, with deep enough snow, to survive the summer melt. While snow accumulation would have persisted through summer, the deep snow, and high levels of snow ice formation in the ice core data suggest very high accumulation rates along the coast. This is also supported by circumpolar snowfall estimates [e.g., *Giovinetto and Bentley*, 1985] and atmospheric reanalysis [*Maksym and Markus*, 2008].

The regional variability in snow depth distribution suggested by Figures 11 and 12 is plausible. The area around the Abbot ice shelf and westward into the Amundsen Sea is a region of persistent multiyear ice. This is clearly seen in Envisat SAR imagery from summer (not shown here), 2009—the only ice to survive the summer in the southern Bellingshausen/Amundsen is found in this region. The coastal current in the southern Bellingshausen Sea will also tend to transport ice westward to this region through the winter [e.g., *Assmann et al*., 2005], thus, we expect thick ice with a deep snow cover to be found in this area, with younger ice with a thinner snow cover to the east. This is suggested in Figure 12, with the deepest snow and largest freeboards found here in 2010 (with the exception of higher freeboards in the multiyear ice region of the northwestern Weddell Sea). To the east, thinner snow is observed in the OIB data, consistent with greater ice export and thinner ice. Note in 2011, snow depths and freeboards are somewhat less, consistent with Envisat SAR imagery (not shown here) that suggest there should be less multiyear or deformed ice in this region.

We suggest that, through a combination of ice persistence in coastal regions, heavy deformation caused by northerly winds [e.g., *Massom et al*., 2006, 2008], and heavy snowfall along the Antarctic coast [e.g., *Maksym and Markus*, 2008], thick ice with heavy snow cover is widespread along the Bellingshausen Amundsen coast, and that these conditions have up to now made these areas inaccessible to icebreakers. These data suggest that snow depth (and ice thickness) may be substantially thicker in many regions than in situ data to date indicate.

6.3. Snow Depth and ATM Surface Roughness

Overall, we find correlations of 0.71–0.84 between snow depth and snow surface roughness (at 4 km length scale), consistent with the fact that deformed ice tends to trap deeper snow [e.g., *Worby et al*., 2008a; *Markus et al*., 2011]. Heavily deformed areas become catchments for snow; hence ridged areas tend to have a thicker snow cover. The regression slope between the two parameters is informative: it ranges from 0.83 to 1.25 in the Weddell Sea and 1.36 to 1.70 in the Bellingshausen Sea. The scatter in the two parameters (see Figures 6, 9, and 11) is higher when the surface is rougher and the snow thicker. A lower slope could be associated with the limit of available snow for redistribution to these deformed areas; or, the redistribution forcing could be weaker in those regions. As the slope is generally lower in the Weddell Sea, where precipitation is generally lower and where we expect the redistribution forcing to be stronger [*Leonard and Maksym*, 2011], the former explanation seems most plausible. In the opposite, a higher slope could mean that a deep snow cover smooths the observed snow surface roughness. Evidence of this can be seen in the higher slopes in the Bellingshausen Sea where we find the highest slope over the thickest snow seen in our surveys. Anecdotally, this is consistent with summer field observations in the Bellingshausen and Amundsen Seas, where very deep snow ($\sim$1 m, unpublished data) obscures any ice surface topography. This relationship between snow depth and snow surface roughness could be potentially useful for understanding redistribution and snow depth. Some caution in interpretation of these relationships is warranted. At the

roughness scale of 4 km used here, the surface roughness calculation may incorporate a variety of ice types. As such, the roughness will be a function of both the degree of deformation and the amount of younger, thinner ice within the area. Since snow depth is a strong function of the age of the underlying ice, these relationships may be indicative of the heterogeneity of ice age in addition to snow redistribution.

6.4. Snow Depth and Radar Backscatter

We find correlations of snow depth to backscatter in Envisat (C-band) SAR imagery. The sharp drop in snow depth associated with that tongue of sea ice with lower radar backscatters, that extends from the southern Weddell Sea (see Figure 5) is remarkable. This feature is composed of very level ice (Pers. Comm. C. Haas) that originally formed in the polynya north of the Ronne ice shelf and drifted north over the course of several months. The young age, location of origin (where precipitation is very low), and lack of deformational catchment features all support a thin snow cover. As well, snow depth is correlated to the areas of higher backscatter in the eastern and the northwestern Weddell Sea. The former is most likely an area of enhanced deformation or older ice, indicating snow depth and radar backscatter are related through surface roughness; we demonstrated here that snow depth is correlated to surface roughness, and it is a fact the radar backscatter is sensitive to surface roughness [e.g., *Drinkwater and Lytle*, 1997]. The latter is in an area known for thick, multiyear ice cover with deep snow cover [*Massom et al*., 1997]. Multiyear ice invariably has relatively deep snow cover in the Antarctic, and also exhibits enhanced volume backscatter [*Morris et al*., 1998].

7. Conclusions

The present paper describes and assesses an approach for retrieval of snow depth from the radar data acquired by Operation IceBridge (OIB), examines the results from eight flight lines from the Weddell and Bellingshausen Seas, and compares the snow depth with available field observations. Here, we revisit some of the geophysical results of note and their implications.

In the Weddell Sea, the snow depths reported here are generally higher than the vast majority of those reported from in situ data. As discussed earlier, field observations of snow depth from two sources—underway shipboard observations and mechanical drilling profiles—favor sampling of the thinner end of the snow depth distribution due to physical and logistical constraints. Thus, these sample populations may not be representative of regional statistics. Furthermore, the sea ice cover sampled by the OIB tracks has rarely been surveyed this late in the season, in part because restricted ship accessibility to these areas with thicker ice and snow. By the time of the OIB surveys, the ice cover will have experienced the full season of growth, deformation, and snow accumulation. We attribute the differences seen here, in large part, to spatial sampling constraints inherent in available field measurements and to the lack of observations during spring in much of the study areas. Our snow depth retrievals suggest that much of the region in the interior pack in spring, particularly near the Antarctic Peninsula, has much deeper snow (and, by inference, thicker ice) than has been typically described elsewhere. The regions of heavy deformation and multiyear ice in the western Weddell Sea are undersampled (particularly in spring), and these ice types are well known to possess deep snow covers. For the Bellingshausen Sea, similar issues of sampling (accessibility and time of year) plague the comparison of our retrievals with available field observations. As well, our results also suggest a significantly thicker snow cover near the Antarctic coast. It is also possible, due to the resolution limitations of the radar, that areas of thin snow and ice are undersampled by our retrieval process but this does not preclude the fact that areas of much thicker snow are seen in the data, and therefore, sampling for obtaining regional statistics remain an issue.

The predominant view of the Antarctic ice cover has been informed by available field observations: sea ice freeboards in field observations usually have means very near zero. This observation has been exploited by *Kurtz and Markus* [2012] to determine ice thickness from ICESat retrievals of total freeboard and sea ice volume. Our results suggest that for larger freeboards (presumably either heavily deformed ice or multiyear ice), the total freeboard is significantly larger than the snow depth, and hence, the sea ice freeboard is significant. In this case, other approaches that allow for nonzero ice freeboard may be more appropriate [e.g., *Yi et al*., 2011; *Xie et al*., 2013]. Even for lower freeboards where a linear relationship between total freeboard and snow depth is observed, the snow depth is in most cases significantly less than the total freeboard. If the snow depth and sea ice thickness in the late spring in much of the Weddell, Amundsen, and Bellingshausen Seas were significantly greater than previously thought, it would alter our current view of the

surface heat and energy budget, air/ice/ocean interactions, and mass balance. As well, it will affect future measurement approaches in field programs and remote sensing campaigns.

These results point to the need for better sampling of the Antarctic sea ice cover, so as to better understand the sampling biases in terms of the field observations, which are critically needed for the assessment of the snow radar retrievals and for informing methodologies for conversion of freeboard to thickness. We also note that the ice areas with much of the snow depths and freeboards presented here would be largely impenetrable to most icebreakers, and the accessibility issues remain a challenge to provide adequate sampling of the ice cover.

Acknowledgments
We thank Shirley Pang for her software support throughout this work. The IceBridge snow-radar and ATM data sets used in this paper are available at http://nsidc.org/data/icebridge. R. Kwok carried out this work at the Jet Propulsion Laboratory, California Institute of Technology, under contract with the National Aeronautics and Space Administration. T. Maksym carried out this work at the Woods Hole Oceanographic Institution, under contract with the National Aeronautics and Space Administration.

References

Assmann, K. M., H. H. Hellmer, and S. S. Jacobs (2005), Amundsen Sea ice production and transport, *J. Geophys. Res.*, *110*, C12013, doi:10.1029/2004JC002797.

Drinkwater, M. R., and V. I. Lytle (1997), ERS 1 radar and field-observed characteristics of autumn freeze-up in the Weddell Sea, *J. Geophys. Res.*, *102*(C6), 12,593–12,608.

Eicken, H., M. Lange, H.-W. Hubberten, and P. Wadhams (1994), Characteristics and distribution patterns of snow and meteoric ice in the Weddell Sea and their contribution to the mass balance of sea ice, *Ann. Geophys.*, *12*, 80–93.

Farrell, S. L., N. T. Kurtz, L. Connor, B. Elder, C. Leuschen, T. Markus, D. C. McAdoo, B. Panzer, J. Richter-Menge, and J. Sonntag (2011), A first assessment of IceBridge snow and ice thickness data over Arctic sea ice, *IEEE Trans. Geosci. Remote Sens.*, *50*(6), doi:10.1109/TGRS.2011.2170843.

Giles, K. A., S. W. Laxon, and A. P. Worby (2008), Antarctic sea ice elevation from satellite radar altimetry, *Geophys. Res. Lett.*, *35*, L03503, doi:10.1029/2007GL031572.

Giovinetto, M. B., and C. R. Bentley (1985), Surface balance in ice drainage systems of Antarctica, *Antarct. J., U. S.*, *20*, 6–13.

Haas, C., M. Nicolaus, S. Willmes, A. Worby, and D. Flinspach (2008), Sea ice and snow thickness and physical properties of an ice floe in the western Weddell Sea and their changes during spring warming, *Deep Sea Res., Part II*, *55*, 963–974, doi:10.1016/j.dsr2.2007.12.020.

Haas, C., M. Nicolaus, A. Friedrich, A. Pfaffling, Z. Li, and T. Toyota (2011), Sea ice measurements during POLARSTERN cruise ANT-XXIII/7 (Winter Weddell Outflow Study), doi:10.1594/PANGAEA.771247.

Jeffries, M. O., R. A. Shaw, K. Morris, A. L. Veazey, and H. R. Krouse (1994), Crystal structure, stable isotopes (delta 18O), and development of sea ice in the Ross, Amundsen, and Bellingshausen seas, Antarctica, *J. Geophys. Res.*, *99*(C1), 985–995.

Jeffries, M. O., S. Li, R. A. Jaña, H. R. Krouse, and B. H. Cushing (1998), Late winter first-year ice floe thickness variability, seawater flooding and snow ice formation in the Amundsen and Ross Seas, in *Antarctic Sea Ice: Physical Processes, Interactions and Variability, Antarct. Res. Ser.*, vol. 74, edited by M. O. Jeffries, pp. 69–87, AGU, Washington, D. C.

Kanagaratnam, P., T. Markus, V. Lytle, B. Harvey, P. Jansen, G. Prescott, and P. Gogineni (2007), Ultrawideband Radar Measurements of Thickness of Snow Over Sea Ice, *IEEE Trans. Geosci. Remote Sens.*, *45*(9), 2715–2724, doi:10.1109/TGRS.2007.900673.

Koenig, L., S. Martin, M. Studinger, and J. Sonntag (2010), Polar airborne observations fill gap in satellite data, *Eos Trans. AGU*, *91*(38), 333–334, doi:10.1029/2010eo380002.

Krabill, W. B., W. Abdalati, E. B. Frederick, S. S. Manizade, C. F. Martin, J. G. Sonntag, R. N. Swift, R. H. Thomas, J. G. Yungel (2002), Aircraft laser altimetry measurement of elevation changes of the Greenland ice sheet: Technique and accuracy assessment, *J. Geodyn.*, *34*, 357−376.

Kurtz, N. T., and S. L. Farrell (2011), Large-scale surveys of snow depth on Arctic sea ice from Operation IceBridge, *Geophys. Res. Lett.*, *38*, L20505, doi:10.1029/2011GL049216.

Kurtz, N. T., and T. Markus (2012), Satellite observations of Antarctic sea ice thickness and volume, *J. Geophys. Res.*, *117*, C08025, doi:10.1029/2012JC008141.

Kurtz, N. T., et al. (2013), Sea ice thickness, freeboard, and snow depth products from Operation IceBridge airborne data, *Cryosphere*, *7*, 1035–1056, doi:10.5194/tc-7–1035-2013.

Kwok, R., J. C. Curlander, R. McConnell, and S. Pang (1990), An ice motion tracking system at the Alaska SAR facility, *IEEE J. Oceanic Eng.*, *15*(1), 44–54.

Kwok, R., B. Panzer, C. Leuschen, S. Pang, T. Markus, B. Holt, and S. Gogineni (2011), Airborne surveys of snow depth over Arctic sea ice, *J. Geophys. Res.*, *116*, C11018, doi:10.1029/2011JC00737.

Kwok, R., G. F. Cunningham, S. S. Manizade, and W. B. Krabill (2012), Arctic sea ice freeboard from IceBridge acquisitions in 2009: Estimates and comparisons with ICESat, *J. Geophys. Res.*, *117*, C02018, doi:10.1029/2011JC007654.

Leonard, K. C., and T. Maksym (2011), The importance of wind-blown snow redistribution to snow accumulation on Bellingshausen Sea ice, *Ann. Glaciol.*, *52*(57), 271–278.

Lewis, M. J., J. L. Tison, B. Weissling, B. Delille, S. F. Ackley, F. Brabant, and H. Xie (2011), Sea ice and snow cover characteristics during the winter-spring transition in the Bellingshausen Sea: An overview of SIMBA 2007, *Deep Sea Res., Part II*, *58*, 1019–1038 doi:10.1016/j.dsr2.2010.10.027.

Maksym, T., and M. O. Jeffries (2000), A one-dimensional percolation model of flooding and snow ice formation on Antarctic sea ice, *J. Geophys. Res.*, *105*(C11), 26,313–26,331.

Maksym, T., and T. Markus (2008), Antarctic seas ice thickness and snow-to-ice conversion from atmospheric reanalysis and passive microwave snow depth, *J. Geophys. Res.*, *113*, C02S12, doi:10.1029/2006JC004085.

Maksym, T., S. E. Stammerjohn, S. Ackley, and R. Massom (2012), Antarctic sea ice-A polar opposite?, *Oceanography*, *25*(3), 140–151.

Markus, T., R. Massom, A. Worby, V. Lytle, N. Kurtz, and T. Maksym (2011), Freeboard, snow depth, and sea ice roughness in East Antarctica from in-situ and multiple satellite data, *Ann. Glaciol.*, *52*(57), 242–248.

Massom, R. A., M. R. Drinkwater, and C. Haas (1997), Winter snow cover on sea ice in the Weddell Sea, *J. Geophys. Res.*, *102*(C1), 1101–1117.

Massom, R. A., et al. (2001), Snow on Antarctic sea ice, *Rev. Geophys.*, *39*(3), 413–445.

Massom, R. A., et al. (2006), Extreme anomalous atmospheric circulation in the West Antarctic Peninsula region in austral spring and summer 2001/02, and its profound impact on sea ice and biota, *J. Clim.*, *19*, 3544–3571.

Massom, R. A., S. E. Stammerjohn, W. Lefebvre, S. A. Harangozo, N. Adams, T. A. Scambos, M. J. Pook, and C. Fowler (2008), West Antarctic Peninsula sea ice in 2005: Extreme ice compaction and ice edge retreat due to strong anomaly with respect to climate, *J. Geophys. Res.*, *113*, C02S20, doi:10.1029/2007JC004239.

Massonnet, F., P. Mathiot, T. Fichefet, H. Goosse, C. König Beatty, M. Vancoppenolle, and T. Lavergne (2013), A model reconstruction of the Antarctic sea ice thickness and volume changes over 1980–2008 using data assimilation, *Ocean Modell.*, *64*, 67–75.

Morris, K., M. O. Jeffries, and S. Li (1998) Sea ice characteristics and seasonal variability of Ers-1 Sar backscatter in the Bellingshausen sea, in *Antarctic Sea Ice: Physical Processes, Interactions and Variability, Antarct. Res. Ser.*, vol. 74, edited by M. O. Jeffries, pp. 213–242, AGU, Washington, D. C.

Nicolaus, M., C. Haas, and S. Willmes (2009), Evolution of first- and second-year snow properties on sea ice in the Weddell Sea during spring-summer transition, *J. Geophys. Res.*, *114*, D17109, doi:10.1029/2008JD011227.

Ozsoy-Cicek, B., S. Ackley, H. Xie, D. Yi, and J. Zwally (2013), Sea ice thickness retrieval algorithms based on in situ surface elevation and thickness values for application to altimetry, *J. Geophys. Res.*, *118*, 3807–3822, doi:10.1002/jgrc.20252.

Panzer, B., D. Gomez-Garcia, C. Leuschen, J. Paden, F. Rodrigues-Morales, A. Patel, T. Markus, B. Holt, and S. Gogineni (2013), An ultra-wideband, microwave radar for measuring snow thickness on sea ice and mapping near-surface internal layers in polar firn, *J. Glaciol.*, *59*(214), 244–254, doi:10.3189/2013JoG12J128.

Patel, A. (2009), Signal Generation for FMCW Ultra-Wideband Radar, Master's thesis, Dep. of Electr. Eng. and Comput. Sci., Univ. of Kansas, Lawrence.

Sturm, M., K. Morris, and R. Massom (1998), The winter snow cover of the west Antarctic pack ice: Its spatial and temporal variability, in *Antarctic Sea Ice: Physical Processes, Interactions and Variability, Antarct. Res. Ser.*, vol. 74, edited by M. O. Jeffries, pp. 1–18, AGU, Washington, D. C.

Turner, J., T. J. Bracegirdle, T. Phillips, G. J. Marshall, and J. S. Hosking (2013), An initial assessment of Antarctic sea ice extent in the CMIP5 models, *J. Clim.*, *26*, 1473–1484, doi:10.1175/JCLI-D-12-00068.1.

Vaughan, D. G., et al. (2013), Observations: Cryosphere, in *Climate Change 2013: The Physical Science Basis*, Contribution of Working Group I to the Fifth Assessment Report of the Intergovernmental Panel on Climate Change, edited by T. F. Stocker et al., Cambridge Univ. Press, Cambridge, U. K.

Willatt, R., S. W Laxon, K. Giles, R. Cullen, C. Haas, and V. Helm (2011), Ku-band radar penetration into snow cover Arctic sea ice using airborne data, *Annals of Glaciology*, *52*(57), 197–205, doi:10.3189/172756411795931589.

Williams, G. D., et al. (2013), Beyond point measurements: Sea ice floes characterized in 3-D, *Eos Trans. AGU*, *94*(7), 69–70.

Wilyard, R. (2006), Airborne radar for measuring snow thickness over sea ice, *CReSIS Tech. Rep. 108*, p. 90, University of Kansas, Lawrence, Kans.

Winebrenner, D. P., E. Nelson, R. Colony, and R. West (1994), Observation of melt onset on multiyear Arctic sea ice using ERS-1 synthetic aperture radar, *J. Geophys. Res.*, *22*(99), 22,425–22,441.

Worby, A. P., M. O. Jeffries, W. F. Weeks, K. Morris, and R. Jaña (1996), The thickness distribution of sea ice and snow cover during late winter in the Bellingshausen and Amundsen seas, Antarctica, *J. Geophys. Res.*, *101*(C12), 28,441–28,455.

Worby, A. P., T. Markus, A. Steer, V. I. Lytle, and R. Massom (2008a), Evaluation of AMSR-E snow depth product over East Antarctic sea ice using in situ measurements and aerial photography, *J. Geophys. Res.*, *113*, C05S94, doi:10.1029/2007JC004181.

Worby, A. P., C. A. Geiger, M. J. Paget, M. L. Van Woert, S. F. Ackley, and T. L. DeLiberty (2008b), Thickness distribution of Antarctic sea ice, *J. Geophy. Res.*, *113*, C05S92, doi:10.1029/2007JC004254.

Xie, H., A. E. Tekeli, S. F. Ackley, D. Yi, and H. J. Zwally (2013), Sea ice thickness estimations from ICESat Altimetry over the Bellingshausen and Amundsen Seas, 2003–2009, *J. Geophys. Res.*, *118*, 2438–2453, doi:10.1002/jgrc.20179.

Yi, D., H. J. Zwally, and J. Robbins (2011), ICESat observations of seasonal and interannual variation of sea-ice freeboard and estimated thickness in the Weddell Sea, Antarctica, *Ann. Glaciol.*, *52*(57), 43–51.

Zhang, J. (2014), Modeling the impact of wind intensification on Antarctic sea ice volume, *J. Clim.*, *27*, 202–214, doi:10.1175/JCLI-D-12–00139.1.